

¹ Importance of considering near-surface attenuation in earthquake source
² parameter estimation: Insights from Kappa at a dense array in Oklahoma

³ Hilary Chang^{*1}, Rachel E. Abercrombie², and Nori Nakata^{1,3}

⁴

ABSTRACT

Separating earthquake source spectra from propagation effects is challenging. The propagation effect contains a site-dependent term related to the high attenuation of shallow sediments. Neglecting the site-dependent attenuation can cause large biases and scattering in the corner frequency (f_c) estimates, resulting in significant stress drop deviations. In this study, we investigate shallow attenuation at the LArge-n Seismic Survey in Oklahoma (LASSO) and site-related biases and scattering in source parameter measurements due to simplified attenuation models. We measure the high-frequency spectral decay parameter kappa on the vertical acceleration spectra of regional earthquakes (125 km away). The site-dependent kappa ($\kappa_{0,acc}$) suggests that attenuation increases rapidly at shallow depth and is highly site-dependent. 10 – 75% of the total attenuation is site-dependent for S waves and is even larger for P waves. The Quality Factor for S waves (Q_s) ranges from 10 to 100 in the upper 400 m. Q_p for P waves is mostly below 10 within the same depth. The Quaternary sediments tend to be more attenuating ($Q_s < 30$) but the Permian rocks also can have high attenuation. We demonstrate that using a non-site-dependent attenuation model in single-spectra fitting leads to large scattering in f_c estimates among stations with apparent good fits. The apparent f_c can significantly deviate when the range of site-dependent kappa is large or with a higher assumed source spectral fall-off rate n . The biases in apparent f_c depend on site condition and distance; however, the correlation between f_c and these factors might not be obvious, depending on model assumptions. We demonstrate that an apparent scaling relation in a previous study for local microearthquakes ($1.3 < M_w < 3.0$) can be largely removed by including a site term, restricting to sites on the higher Q formations, and fixing n . This study highlights the importance of considering near-surface attenuation when modeling source parameters.

¹ Department of Earth, Atmospheric, and Planetary Sciences, Massachusetts Institute of Technology, Cambridge, Massachusetts, 02139, USA; ² Department of Earth and Environment, Boston University, Boston, Massachusetts, 02215, USA; ³ Lawrence Berkeley National Laboratory, Berkeley, California, 94720, USA

KEY POINTS

- Attenuation is dominantly site-dependent in the Central United States.
- Neglecting shallow attenuation causes large uncertainties and biases despite apparently small model misfits.
- Having controlled site conditions is more important than using many stations in estimating source parameters.

Supplemental Material

6 INTRODUCTION

7 An earthquake seismogram contains source effects convolved with propagation effects:

$$u(f) = s(f) \cdot p(f) \cdot g(f), \quad (1)$$

8 where f is frequency, $u(f)$ is the recorded particle displacement, velocity, or acceleration spectrum, $s(f)$ is the source model, $p(f)$ is the path term that describes 9 the path-dependent attenuation, and $g(f)$ is the site-dependent term. The site term 10 is associated with, for example, shallow unconsolidated sediments that have higher 11 attenuation and resonance effects. Incorrect separation of the path and site terms can 12 bias measurements of source parameters such as stress drop ([Abercrombie, 1995](#)). 13

14 Earthquake stress drop characterizes the energy released and is an important parameter 15 for understanding source physics, rupture simulation, and ground motion modeling. However, the stress drop not only depends on how it is defined ([Atkinson 16 and Beresnev, 1997](#); [Ji et al., 2022](#)), but the measurements are also highly variable 17 ([Allmann and Shearer, 2009](#); [Cocco et al., 2016](#); [Abercrombie et al., 2016](#); [Oth et al., 18 2017](#)). The stress drop estimates can deviate for moderate to small events due to 19

*Corresponding author: hilarych@mit.edu

Cite this article as Chang, H., R.E. Abercrombie, and N. Nakata (2022). Importance of considering near-surface attenuation in earthquake source parameter estimation: Insights from Kappa at a dense array in Oklahoma, *Bull. Seismol. Soc. Am.* **XX**, 1–47, doi: [00.0000/0000000000](#).

© Seismological Society of America

the resolution limit, which then causes apparent breakdowns in earthquake self-similarity (Abercrombie, 1995, 2021). The recent Community Stress Drop Validation Project (Baltay et al., 2024; Abercrombie et al., 2024) has revealed highly variable measurements for the 2019 Ridgecrest earthquake sequence among different research teams. They found that the stress drop estimates vary due to methods and assumptions (Abercrombie et al., 2024; Shearer et al., 2024). While many of the research teams observed an increase in stress drops with earthquake magnitude, the observations are still within the range of uncertainty of a constant stress drop. Whether the observed earthquake scaling is due to method biases, simplified assumptions, or actual indications of non-self-similarity is still under debate.

One of the biggest uncertainties in stress drop estimates comes from the corner frequency (f_c) (Abercrombie, 2021). Earthquake stress drops for a circular crack can be modeled as (Eshelby, 1957; Brune, 1970; Madariaga, 1976):

$$\Delta\sigma = \frac{7}{16} \left(\frac{f_c}{k\beta} \right)^3 M_0, \quad (2)$$

where f_c relates to the source dimension, M_0 is the seismic moment, k is a constant depending on the wave type and the rupture model, and β is the shear-wave velocity at the source focal depth. f_c is highly sensitive to the shape of the earthquake spectra and exhibits a notorious trade-off with attenuation (Anderson, 1986; Boore, 1986; Ko et al., 2012). The uncertainty in f_c is magnified by the power of three (Equation 2), causing significant biases in the calculated stress drop and apparent scaling relations between earthquake size and source dimension (Abercrombie, 1995).

There are several approaches to address propagation effects in source spectra modeling. The single-spectra method models the earthquake spectra directly with assumed attenuation structures (e.g., [Ko et al., 2012](#); [Supino et al., 2019](#)). The single-spectra method can be difficult because of irregularities on the spectra and limited bandwidth ([Shearer, 2009](#)), and is subject to parameter trade-offs ([Ko et al., 2012](#)). Another method is the spectral-ratio, the Empirical Green's Functions (EGFs) approach. The spectral-ratio method uses co-located small events with the same focal mechanism as the EGFs to remove propagation effects ([Hartzell, 1978](#); [Hough, 1997](#); [Mayeda et al., 2007](#); [Abercrombie, 2015](#)), and has been shown to be quite effective (e.g., [Chang et al., 2023](#)). The advantage of using EGF is that we do not need to assume an attenuation model. However, a qualified small event is often not available (especially for microearthquakes), and the selection and modeling of the small event brings in other uncertainties ([Abercrombie, 2015](#); [Shearer et al., 2019](#)). Large-scale inversion methods, including the Generalized Inversion Technique (GIT; [Andrews, 1986](#); [Castro et al., 1990](#); [Hartzell, 1992](#); [Oth et al., 2011](#); [Bindi et al., 2020](#)), and spectral decomposition (e.g., [Shearer et al., 2006, 2019](#)), derive non-parametric site response spectra to correct the relative source spectra obtained from an inversion. However, for the source, path, and site terms to be properly constrained in the inversion, a dataset with these terms well-traversed in the parameter space is required. Also, the inversion still suffers from parameter trade-offs ([Shearer et al., 2019](#); [Bindi et al., 2023, 2024](#)), including between f_c , M_0 , $\Delta\sigma$, the high-frequency fall-off rate, and attenuation.

Both the single-spectra method and the spectral decomposition require some assumptions on the attenuation model. In this study, we focus on the single-spectra

approach to investigate the trade-off between f_c and attenuation in source spectral modeling when using an oversimplified attenuation model. We note that this trade-off can occur not only in the single-spectra approach but also in any approach that requires assuming the attenuation model for modeling the earthquake spectra.

The single-spectra approach models the farfield earthquake displacement spectrum and the attenuation as (Ω_t) (Brune, 1970; Boatwright, 1978, 1980):

$$\Omega_t(f) = \frac{\Omega_0}{[1 + (f/f_c)^{\gamma n}]^{1/\gamma}} \cdot e^{-\pi f \kappa}, \quad (3)$$

where Ω_0 is the long-period spectral amplitude, n is the high-frequency fall-off rate, and γ is 1 or 2 depending on whether using a Brune or Boatwright model. The exponential term characterizes the frequency-dependent path effect (Anderson and Hough, 1984).

The attenuation parameter kappa (κ) is the integration of travel time (tt_i) divided by a Quality Factor (Q_i , assumed to be frequency-independent) across each layer i along the propagation path (Hough and Anderson, 1988):

$$\kappa = \int_{path} \frac{tt_i}{Q_i}. \quad (4)$$

A tempting (but often wrong) assumption is that κ is nearly proportional to travel time. For example, the single-spectra fitting approaches in Supino et al. (2019) and Kemna et al. (2020, 2021) assumed attenuation is travel time divided by a constant Q , without a site-dependent attenuation term. This simplification raises concerns because attenuation along the path is often far from evenly distributed.

While the average crustal Q is in the range of hundreds to thousands (Singh and Herrmann, 1983; Benz et al., 1997; Levandowski et al., 2021), the near-surface layers

generally have a much lower Q . Borehole data in California (Jongmans and Malin, 1995; Abercrombie, 1999) and Switzerland (Bethmann et al., 2012) showed Q less than 30 in the top 0.5 km. Abercrombie (1997) found that in the Cajon Pass borehole in California, 90% of the attenuation for earthquakes with an epicentral distance under 15 km occurs in the upper 3 km, while half of the attenuation occurs in the upper 300 m. We will show that neglecting the site-dependent term in κ can result in large scattering and bias.

The LArge-n Seismic Survey in Oklahoma (LASSO; Figure 1; Dougherty et al., 2019), with 1825 vertical-component nodal geophones, provides an unprecedented dataset to examine the site conditions and source parameter variabilities. The dense station coverage with large (moment magnitude $M_w > 3$) distant events that are relatively equidistant from the stations allows a thorough investigation of the apparent attenuation on a flat basin plain. We measure the kappa on the acceleration spectra (denoted as κ_{acc}) of the large distant earthquakes. The site-dependent part of kappa ($\kappa_{0,acc}$) relates to site properties such as the average shear-wave velocity in the top 30 m (V_{s30} ; e.g., Van Houtte et al., 2011) and is an important parameter in ground motion modeling (PEER, 2015).

We use $\kappa_{0,acc}$ to estimate the apparent site attenuation that might apply to the spectra of local earthquakes. Our approach avoids narrow-band amplifications. However, we do not attempt to fully quantify the potential broadband amplification (e.g., Boore and Joyner, 1997; Campbell and Bozorgnia, 2014) and attenuation in the kappa values. We compare the kappa values with the source parameters of local microearthquakes ($M_w < 3$) estimated using the single-spectra method from a previous study (Kemna

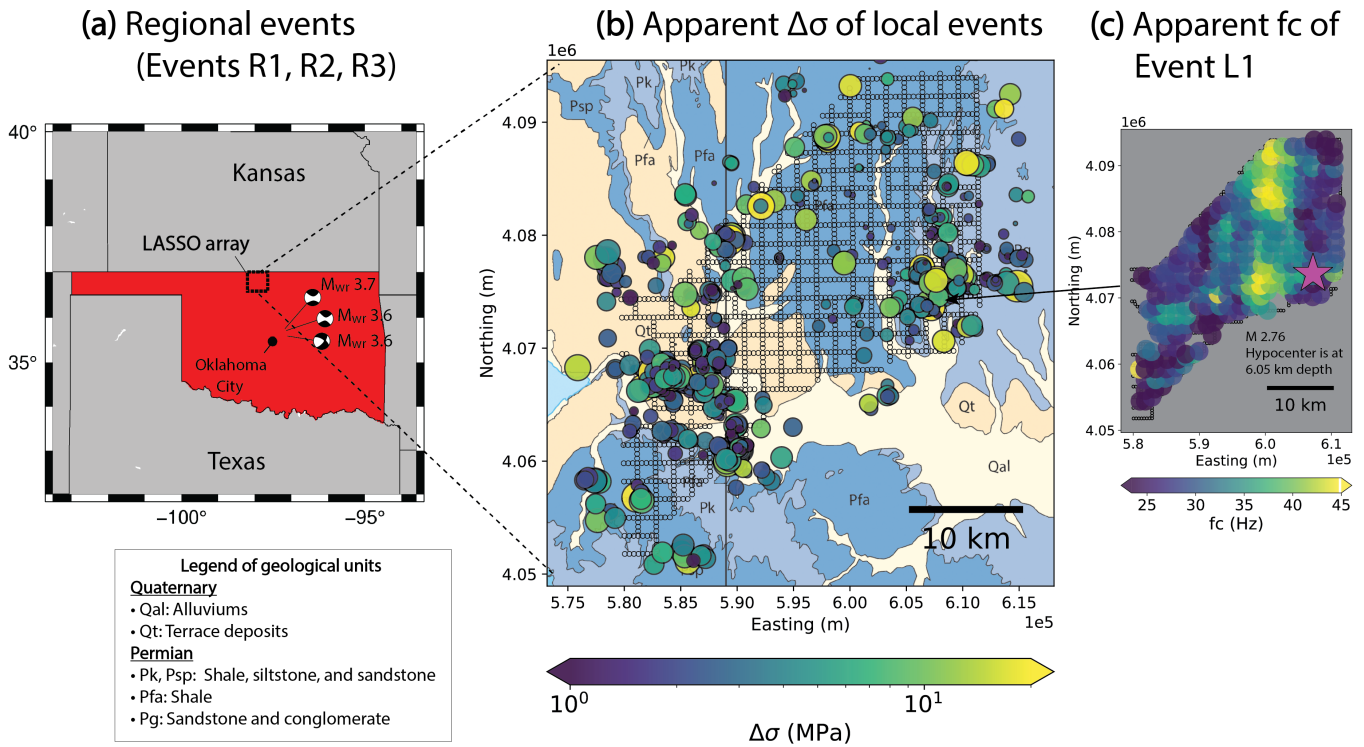


Figure 1: Regional and local earthquakes recorded at the LASSO array and the variability of source parameter measurements using a single-spectra fitting approach. In (a), the focal mechanisms the moment magnitudes (M_{wr}) are the three largest regional earthquakes (event R1, R2, R3) that are 126 – 178 km from the array. The small dashed box marks the array location. In (b), the colored circles are local events. The colors indicate apparent stress drop ($\Delta\sigma$) based on the single-spectra measurements in Kemna et al. (2020) (denoted as KN20). The size of the circles is proportional to local magnitudes (0.01 – 3.0). The small black circles are stations. The map shows the surface geology (see legend on the lower left; Heran et al., 2003). In (c), we show the corner frequency (f_c) estimates using the single-spectra approach for a local event (event L1; the magenta star marks the epicenter) in KN20. Each colored dot in (c) represents the median f_c measured by a subarray that includes stations within a 2.5 km diameter circle.

et al., 2020). We show that the source parameter variabilities can be reproduced using our independent kappa measurements from distant events.

107 LASSO ARRAY AND THE DATA

108 The LASSO array is located on a flat plain in the northern Anadarko Basin, with less than 100 m relief in total (Crain and Chang, 2018). Sedimentary rocks from the Permian to Cambrian ages consist of the top 2 km (Johnson and Luza, 2008). The Quaternary alluvium and terrace deposits cover locally with a thickness of a few to tens of meters (Figure 1b; Heran et al., 2003). The array contains 1825 stations in an area of 25 km

x 32 km with a minimum station spacing of 400 m. The stations are velocity sensors, the Fairfield Nodal vertical-component 10 Hz nodes, with a sampling rate of 500 Hz. The array was deployed from mid-April to mid-May in 2016 for about a month, during which it recorded more than a thousand microearthquakes associated with wastewater injections with local magnitudes ranging from 0.01 to 3.0 (Cochran et al., 2020). The majority of these events occurred between 1.5 and 5.5 km in depth. The array also recorded a few distant events from Central Oklahoma with $M_w > 3.6$ (Figure 1a; 126 – 178 km away; Table S2; U.S. Geological Survey).

Kemna et al. (2020) (denoted as KN20 thereafter) used both a single-spectra fitting approach (Equation 3) and a spectral ratio approach to calculate source parameters, including corner frequency (f_c), seismic moment (M_0), and stress drop ($\Delta\sigma$). While their spectral-ratio method results do not show an apparent scaling relation or biases, the single-spectra method results do, with the biases in f_c and $\Delta\sigma$ correlated with superficial geology (Figure 1b,c; Chang et al., 2023). Both methods exhibit large scattering among stations. Chang et al. (2023) attempted to correct the apparent bias in the single-spectra results using surface ground motions as a proxy; however, large scattering with unknown causes remains after the correction. In their single-spectra approach, KN20 assumed $\kappa = tt/Q$. They performed a grid search to find a combination of $Q = 600$ and $n = 3.5$ that yielded the overall best fit. They used either the Brune ($\gamma = 1$) or the Boatwright model ($\gamma = 2$) depending on which fits better. Later, we will find out the cause of the large scattering with synthetic tests using these fitting criteria.

The large number of stations (nearly 2,000) means that we can group them into sub-arrays to improve stability and resolution, and still retain significant spatial variation.

¹³⁶ We group the stations into 272 subarrays. Each subarray consists of stations within a
¹³⁷ circle of 2.5 km diameter (15 – 20 stations). In the following analysis, we stack spectra
¹³⁸ in each subarray and take the median measurements from KN20 among the stations
¹³⁹ in a subarray. The spectra and data points in the figures represent averaged values in
¹⁴⁰ subarrays instead of individual stations. By averaging among stations, we reduce the
¹⁴¹ impact of local resonances and outliers.

¹⁴² SHALLOW ATTENUATION ACROSS THE LASSO ARRAY

¹⁴³ We estimate the high-frequency spectral decay parameter κ_{acc} on the Fourier acceleration
¹⁴⁴ spectra based on [Anderson and Hough \(1984\)](#):

$$\kappa_{acc} = -\frac{1}{\pi} \frac{d(\ln(A))}{df}, \quad (5)$$

¹⁴⁵ where $\frac{d(\ln(A))}{df}$ is the slope of the acceleration spectrum in linear-log space and has a unit
¹⁴⁶ of seconds. The measured κ_{acc} has a site-dependent component $\kappa_{0,acc}$ and a distance-
¹⁴⁷ dependent component $\kappa_{r,acc}$. The site component $\kappa_{0,acc}$ can be derived by removing a
¹⁴⁸ linear dependence between κ_{acc} and epicentral distances ([Ktenidou et al., 2015](#)).

¹⁴⁹ We use three regional earthquakes in Central Oklahoma (local magnitude $M_L = 3.6 -$
¹⁵⁰ 3.7; R1 – R3 in Table S2) to estimate $\kappa_{p,acc}$ for P arrivals and $\kappa_{s,acc}$ for S arrivals. To calcu-
¹⁵¹ late the Fourier acceleration spectra, we first demean, detrend, taper, prefilter, remove
¹⁵² the instrument response, and convert the raw data to acceleration using Obspy with the
¹⁵³ response file provided by the manufacturer. We put a water level of 40 to avoid amplify-
¹⁵⁴ ing noise below 1 Hz when removing the responses. After the data conversion, we cut
¹⁵⁵ the 1.5 s window starting at 0.15 s before the arrivals. A short time window can avoid
¹⁵⁶ scattering effects that would result in an underestimated attenuation ([Parolai et al.,](#)

¹⁵⁷ 2022). The arrivals are estimated using the similar approach in Chang et al. (2023): We
¹⁵⁸ first estimate the arrivals by raytracing with the velocity model from Rubinstein et al.
¹⁵⁹ (2018). Then, we visually examine the predicted moveout and adjust small time shifts
¹⁶⁰ of the arrival for each event. The amplitude spectra are calculated using the multitaper
¹⁶¹ method (Prieto, 2022). See Text S1 for more details on data processing.

¹⁶² It is important to measure kappa beyond the site-amplification resonance peaks and
¹⁶³ the corner frequency of the earthquake source. We follow a similar approach as Nye
¹⁶⁴ et al. (2023) to select the start of the frequency band (Figure 2). First, we fit the accel-
¹⁶⁵ eration spectra with a degree-15 polynomial. Then, we calculate the first derivative of
¹⁶⁶ the polynomial. The minimum of the first derivatives is where the largest amplitude
¹⁶⁷ drop occurs. The start of the frequency band is the minimum of the first derivative
¹⁶⁸ (Nye et al., 2023), or 1.5 times the corner frequency (Ktenidou et al., 2016), depend-
¹⁶⁹ ing on which one is higher. Events R1 – R3 have corner frequencies between 2 – 5 Hz
¹⁷⁰ based on spectra observed on the rock sites. The end of the frequency band is where the
¹⁷¹ signal-to-noise ratio (SNR) drops below 3 (Ktenidou et al., 2016). The SNR is defined
¹⁷² as the ratio between the spectral amplitude of the signal to that of the noise, which is
¹⁷³ calculated in a 1.5 s window, 8 s before the P arrivals. The majority of $\kappa_{p,acc}$ are mea-
¹⁷⁴ sured between 10 – 30 Hz; and for $\kappa_{s,acc}$, the majority are between 12 – 45 Hz (Figure
¹⁷⁵ S1).

¹⁷⁶ To avoid narrow-band resonances, we require a minimum frequency bandwidth of
¹⁷⁷ 15 Hz, where the spectra show linearly decaying trends on the semi-log scale (Figure
¹⁷⁸ 3). For P waves, sites with higher kappa have lower amplitudes above 20 Hz compared
¹⁷⁹ with other sites. For S waves, sites with higher kappa have higher amplitudes below

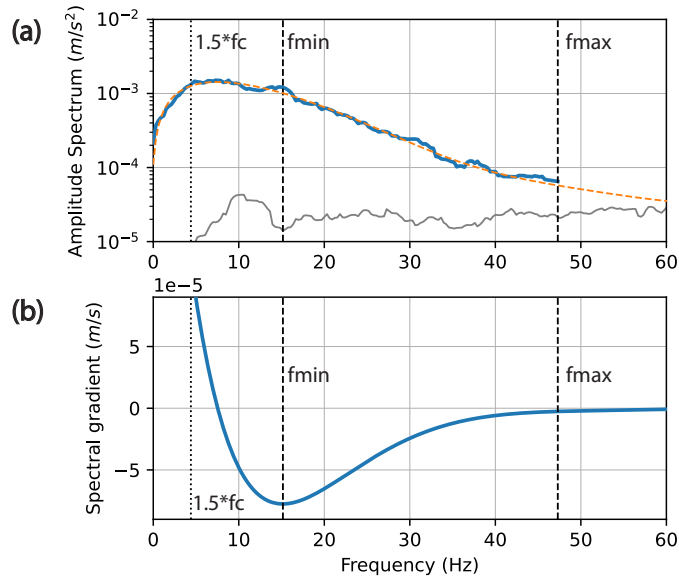


Figure 2: The frequency band selection criteria for measuring kappa (κ_{acc}). In (a), the blue and grey spectra are the acceleration spectra for the S arrival and noise, respectively. The spectra are stacked among stations in the subarray (15 – 20 stations). We fit the spectra with a degree-15 polynomial (orange dashed curve in (a)) and calculate the first derivative of the polynomial (blue curve in (b)). We measure $\kappa_{s,acc}$ on the spectra between f_{min} and f_{max} (vertical dashed lines). f_{min} is at the bottom of the valley of the first derivative. f_{max} is just before where the signal-to-noise ratio starts to drop below 3. We require $f_{min} > 5$ Hz because the corner frequency (f_c) is between 2 – 5 Hz for the 3 regional events.

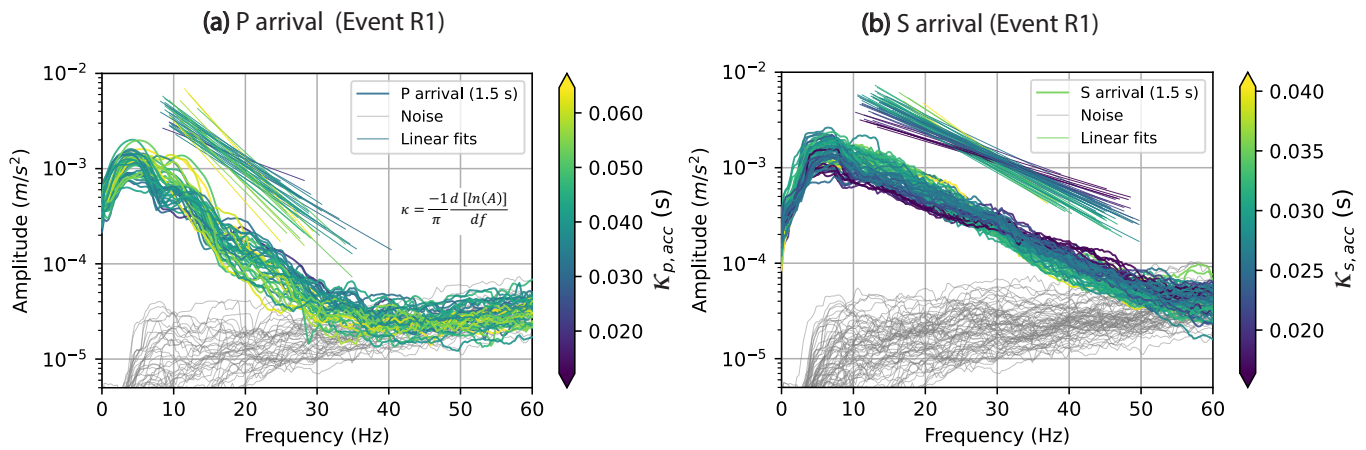


Figure 3: High-frequency spectral decay parameter kappa (κ) measured from the vertical component of the acceleration spectra of regional event R1. (a) P-arrival for $\kappa_{p,acc}$, and (b) S-arrival for $\kappa_{s,acc}$. The spectra are stacked among stations within a subarray of a 2.5 km diameter circle (15 – 20 stations). The signal spectra (colored) are calculated in a 1.5 s window around the P- or S-arrivals. The noise spectra (gray) are calculated in a 1.5 s window that is 8 s before the P arrivals. The thin colored lines are linear fits between amplitude (A) and frequency (f) for estimating kappa. We require a minimum frequency bandwidth of 15 Hz. See the text for the criteria for determining the frequency range. Only one-fourth of the total spectra and fitting are shown (equally spaced across the array) for visualization.

180 25 Hz and lower amplitudes above 30 Hz compared with other sites. The κ_{acc} captures
181 the apparent spectral attenuation that spans a wide frequency range.

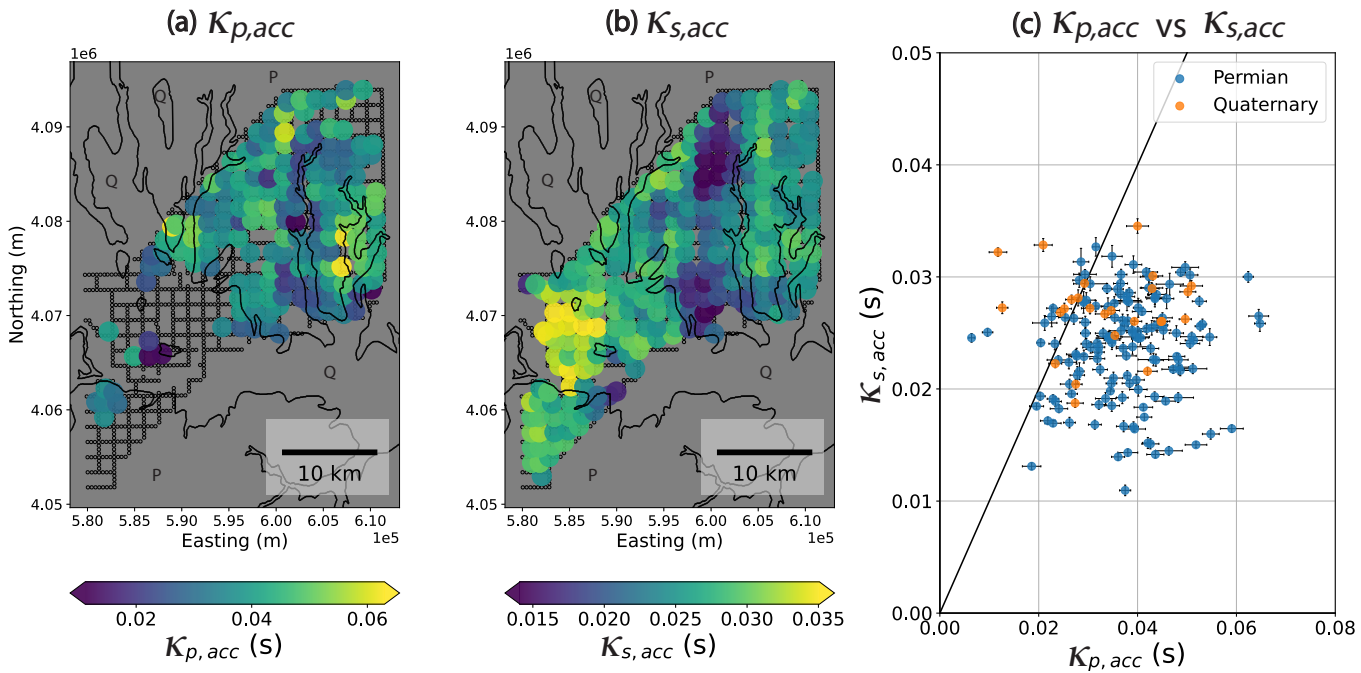


Figure 4: High-frequency spectral decay parameter kappa (vertical component): (a) $\kappa_{p,acc}$ and (b) $\kappa_{s,acc}$, and (c) their comparisons. The kappa values are the median of regional events R1 – R3. In (a) and (b), each colored circle represents a subarray consisting of stations within a 2.5 km diameter circle (15 – 20 stations; small black circles in the background). The color ranges exclude the 1% lowest and highest values for visualization. The contours indicate the boundaries of the surficial Quaternary formations (Q) versus the Permian formations (P). The error bars in (c) are the standard deviation of the fitting. The spectral decay is mostly site-dependent with the Quaternary sediments being more attenuating than the Permian rocks.

Figure 4 shows $\kappa_{p,acc}$ and $\kappa_{s,acc}$ measured from the large distant events. The kappa values are strongly site-dependent. $\kappa_{p,acc}$ is mostly limited to Permian formations (Figure 4a) because of limited bandwidth on the Quaternary sites for P waves. $\kappa_{s,acc}$ shows higher values (> 0.03 s) on the Quaternary formations and on the southwest side of the array (Figure 4b). In Figure 4c, $\kappa_{p,acc}/\kappa_{s,acc} > 1$ in general, which suggests P waves exhibit higher spectral decay than S waves. If we relax the minimum bandwidth to 10 Hz to include more measurements on the Quaternary sites (Figure S2), the higher $\kappa_{p,acc}$ and $\kappa_{s,acc}$ are both on the Quaternary sites and $\kappa_{p,acc}$ and $\kappa_{s,acc}$ have a weak correlation (cross-correlation coefficient = 0.3). However, relaxing the minimum bandwidth to 10 Hz is likely subject to amplitude bulges between 10 and 20 Hz (Figure S3). Hence, we choose to stick to the 15 Hz minimum bandwidth requirement.

¹⁹³ The kappa value consists of a path component ($\kappa_{r,acc}(r)$) and a site component ($\kappa_{0,acc}$)
¹⁹⁴ (Ktenidou et al., 2015):

$$\kappa_{acc} \approx \kappa_{r,acc}(r) + \kappa_{0,acc}. \quad (6)$$

¹⁹⁵ Here, r represents the epicentral distance. We can obtain the site term after removing
¹⁹⁶ the distance-dependent $\kappa_{r,acc}(r)$. According to Ktenidou et al. (2016), a distance of 50
¹⁹⁷ – 100 km is necessary to observe the κ -distance relation in the CEUS, where the crust
¹⁹⁸ has low attenuation. The total epicentral distance (> 125 km) is sufficient to resolve
¹⁹⁹ $\kappa_{r,acc}$. However, the distance difference between subarrays is less than 20 km (< 20%
²⁰⁰ of the total distance), which is too small to resolve the distance-dependence within the
²⁰¹ array (Figure S4). We assume the path term is nearly constant across the array and
²⁰² the path term is represented by the minimum κ_{acc} of the three events (i.e., $\kappa_{r,acc} =$
²⁰³ $\min(\kappa_{acc})$). This gives $\kappa_{r,p,acc} = 0.004$ s for P waves and $\kappa_{r,s,acc} = 0.010$ s for S waves.
²⁰⁴ We estimate the site term $\kappa_{0,acc}$ by subtracting $\min(\kappa_{acc})$ from κ_{acc} . The site-dependent
²⁰⁵ kappa $\kappa_{0,p,acc}$ ranges between 0.002 – 0.060 s (mostly on the Permian rocks) and $\kappa_{0,s,acc}$
²⁰⁶ ranges between 0.001 – 0.030 s (Figure 5). The majority of the Quaternary sites, and
²⁰⁷ many Permian sites, have $\kappa_{0,s,acc} > 0.015$ s. Note that the range of site-dependent kappa
²⁰⁸ is 3 times than the total path-related kappa for S waves and almost 15 times for P waves.
²⁰⁹ The site-related kappa is 10 – 75% of the total kappa for S waves and can be more than
²¹⁰ 90% for P waves.

²¹¹ We examine how the site-dependent $\kappa_{0,s,acc}$ relates to ground motions at different
²¹² frequency bands. We calculate the Root-Mean-Square (RMS) amplitudes for S waves
²¹³ for the regional earthquakes. The RMS amplitudes are calculated in a 5-s time win-

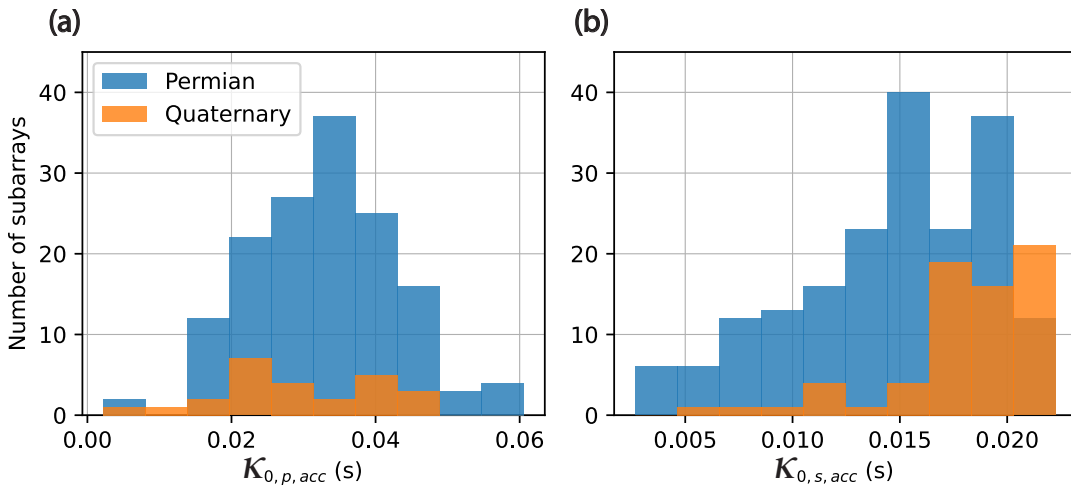


Figure 5: Distribution of the site-dependent kappa estimated (a) for P waves ($\kappa_{0,p,acc}$) and (b) for S waves ($\kappa_{0,s,acc}$), determined using the vertical component of the acceleration spectra of regional events R1 – R3. Blue represents sites on Permian rocks and orange represents those on Quaternary sediments. Note that most Quaternary sites do not have available $\kappa_{0,p,acc}$ because of the high attenuation. The Quaternary sediments have higher $\kappa_{0,s,acc}$ than the Permian rocks.

dow starting from 0.5 s before the S-arrival (similar to Chang et al., 2023, but with a shorter time window). Figure 6a shows that $\kappa_{0,s,acc}$ positively correlates with ground motions below 25 Hz and negatively correlates with ground motions above 30 Hz. Hence, a higher $\kappa_{0,s,acc}$ is both a result of higher amplitudes at lower frequencies and lower amplitudes at higher frequencies. This observation is consistent with the comparison between surface and borehole (2.5 km depth) recordings of earthquake spectra at Cajon Pass, California (Abercrombie and Leary, 1993). The spectrum from their surface station showed relative amplification at lower frequencies and attenuation at higher frequencies. The transition from amplification to attenuation would shift to lower frequencies in regions with higher attenuation.

We examine how $\kappa_{0,s,acc}$ measured from the regional events relates to the corner frequency estimates for the local events in KN20. We select the three of the best recorded local events (L1 – L3; event L1 is shown in Figure 1c). In each event, for each subarray, we calculate the median f_c of individual station estimates in KN20. In Figure 6b,

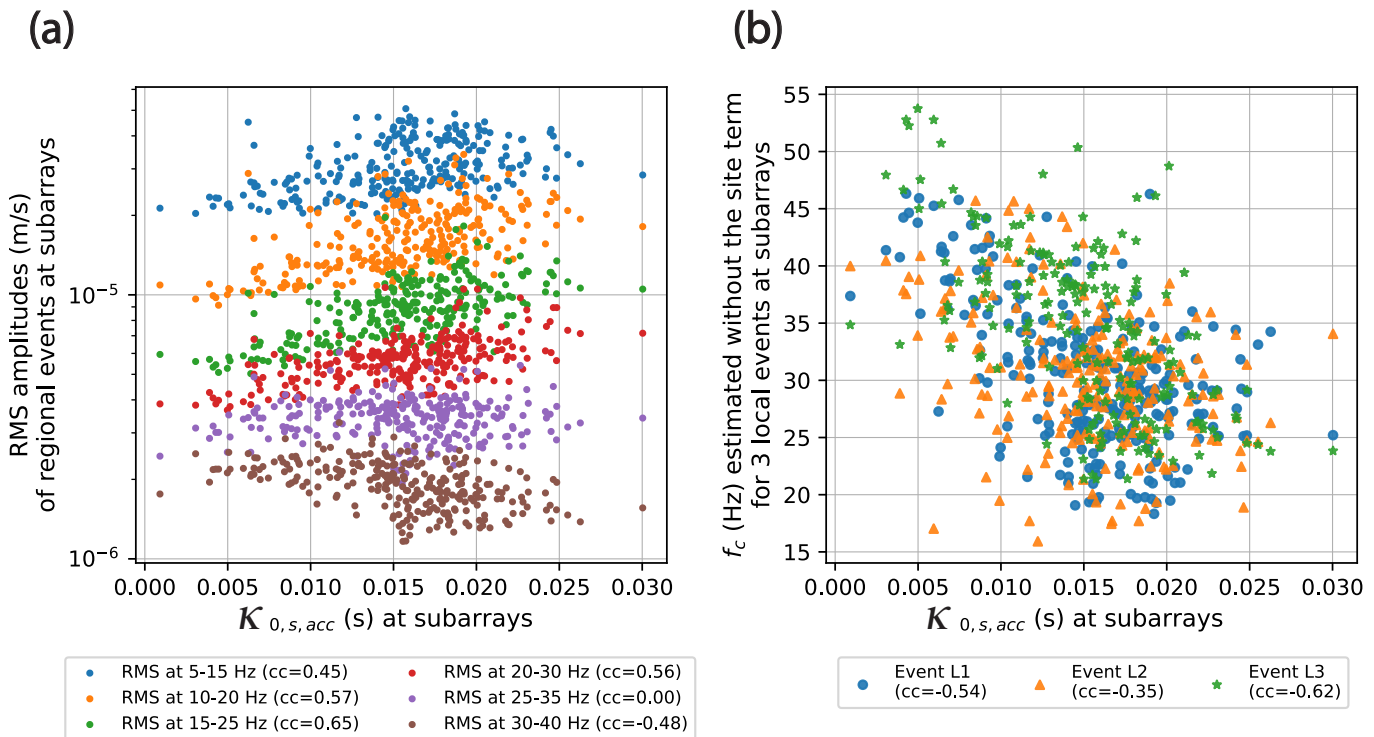


Figure 6: Relationship between site-dependent kappa ($\kappa_{0,s,acc}$) and (a) median vertical ground motion at different frequencies, and (b) corner frequency (f_c) measurements of three local events (L1 – L3) in KN20. The Root-Mean-Square (RMS) amplitude is in the S wave window (5 s after the S arrivals), taking the median among the three regional events (R1 – R3). Each f_c is the median value among 15 – 20 station measurements in a subarray. $\kappa_{0,s,acc}$ is measured on the vertical component. cc is Pearson's cross-correlation coefficient (all non-zero cc have p-values < 5%).

²²⁸ $\kappa_{0,s,acc}$ negatively correlates with the estimated corner frequency in KN20. The correlation between these two independent measurements indicates potential site biases. Our results are consistent with (Shearer et al., 2024, this special issue). They investigated f_c and model attenuation between different methods for two Ridgecrest aftershocks. They found methods that use higher kappa tend to have higher f_c results, which suggests trade-offs between kappa and f_c . Here, our kappa is measured independently from the f_c . The fact that sites with a higher kappa tend to get lower f_c suggests biases due to neglecting site effects under the assumption of $\kappa = tt/Q$ in KN20.

²³⁶ If we assume the site-dependent attenuation is primarily occurring in the upper H m, we can convert the site kappa into average estimates of shallow Q using:

$$Q = \frac{\sum_{i=0}^{i=N} tt_i}{\kappa_{0,acc}}. \quad (7)$$

²³⁸ N is the number of layers with a total thickness of H , above which the site-term primar-
²³⁹ ily occurs. $\sum_{i=0}^{i=N} tt_i$ is the travel time spent in the shallow layers and can be estimated by
²⁴⁰ a velocity model and raytracing. We use the S-wave velocity models from [Rubinstein](#)
²⁴¹ [et al. \(2018\)](#) (for 1.5 km and deeper) and [Chang et al. \(2024\)](#) (for shallower than 1.5
²⁴² km) and assume $V_p = 1.78V_s$ for P-wave velocity ([Catchings, 1999](#)). We estimate the
²⁴³ travel time using the TauP module (using the spherical grid) in Obspy ([Beyreuther](#)
²⁴⁴ [et al., 2010](#)). To determine H , we refer to the previous studies in this region. [Chang](#)
²⁴⁵ [et al. \(2024\)](#) found rapidly decreasing velocity at the shallower depth, with little lateral
²⁴⁶ changes (Figures S5 and S6). There are roughly four known interfaces that likely relate
²⁴⁷ to the shallow attenuation: (1) a few to tens of meters (shallow Quaternary deposits;
²⁴⁸ [Johnson and Luza, 2008](#)), (2) ~ 400 m (rapid velocity transitions) (3) ~ 1.2 km (rapid
²⁴⁹ velocity transitions), and (4) ~ 2.3 km (basin basement; [Crain and Chang, 2018](#)).

²⁵⁰ In this way, if we assume $H = 400$ m, Q_p ranges from 3 – 25 with most (95%) under 10
²⁵¹ and Q_s ranges from 10 – 100 with most under 40 (Figure 7). The Quaternary formations
²⁵² have Q_s less than 30 and only a few very-low Q_p (< 10) available. If we assume $H = 2$
²⁵³ km (near the total depth of the sedimentary basin), we get $Q_p = 10 – 80$ (most under 30)
²⁵⁴ and $Q_s = 40 – 240$ (most under 120) in the top 2 km. Different assumptions for H shift
²⁵⁵ the range of Q_s but do not significantly alter the pattern (Figure S7) because the lateral
²⁵⁶ variations of V_s (and therefore variation of travel time in Equation 7) are small in the
²⁵⁷ top 2 km. Whether H is 100 m or 2 km, the measured Q_s indicates strong attenuation
²⁵⁸ with considerable variability near the surface. In general, we have $Q_p/Q_s < 1$ (Figure

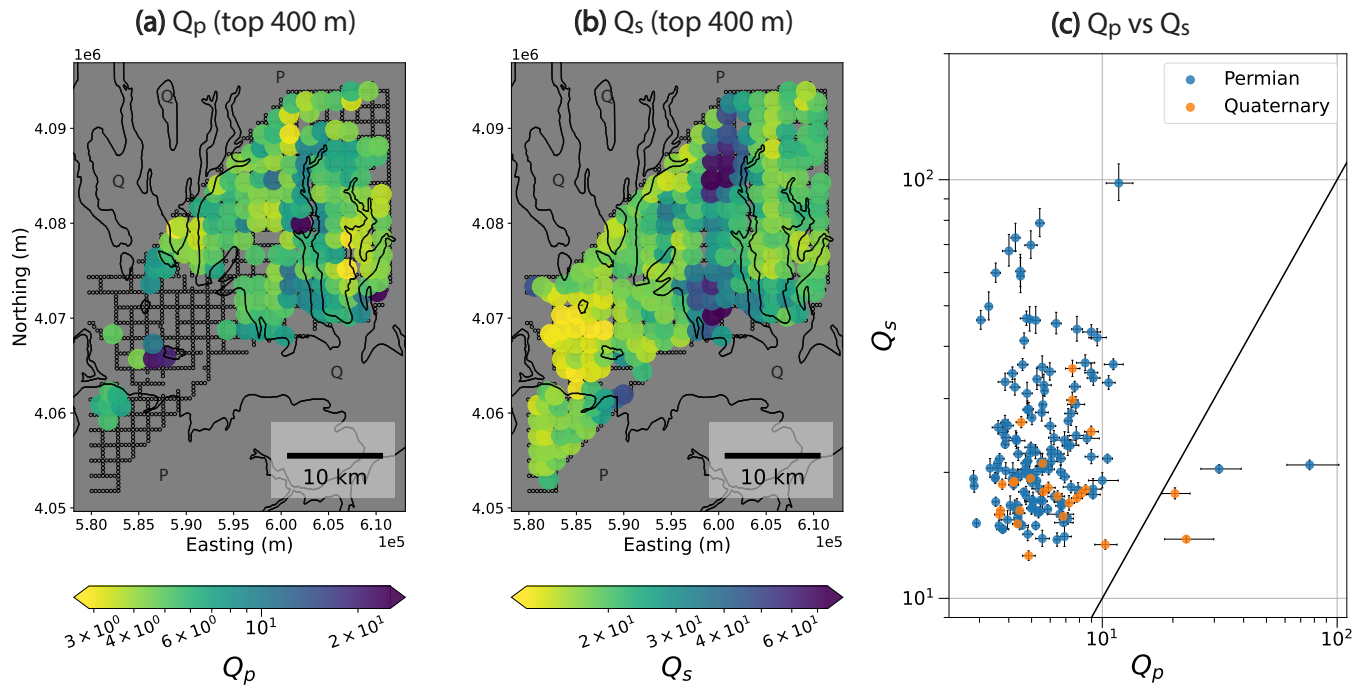


Figure 7: Quality Factors for (a) P waves (Q_p) and (b) S waves (Q_s) in the top 400 m derived using $\kappa_{0,acc}$ (vertical component). (c) Q_p vs Q_s . The Q_p and Q_s are derived from the site spectral decay parameter and the shear-wave velocity structure. The black line in (c) is the 1:1 line. We observe $Q_p/Q_s < 1$, which is expected for partially saturated rocks. See the caption of Figure 4 for other features in the figure.

259 7c) as expected for partially saturated rocks (Toksöz et al., 1979; Hauksson and Shearer,
 260 2006). On the other hand, the Q associated with the path term ($\kappa_{r,acc}$) is more than 3000
 261 (estimated based on P- and S-wave travel times of ~ 20 s and ~ 40 s, respectively), which
 262 is a lot higher compared to the near surface Q .

263 In the next section, we assume Q_s represents site attenuation for both P and S waves
 264 for the local events. This is because we need to characterize the high attenuation on the
 265 Quaternary sites but not many Quaternary sites have available Q_p . This would lead to
 266 a more conservative estimate as Q_p in general is less than Q_s . All investigations are for
 267 the vertical component as the LASSO array does not have the horizontal component.

268 EFFECTS OF IGNORING THE SITE-DEPENDENT SPECTRAL DECAY

269 To investigate the effect of ignoring site-related attenuation, we generate synthetic
 270 displacement spectra and use different assumptions to fit them. We use the source-

271 subarray configuration of local event L1 with the Q values observed in the previous
 272 section. We generate the synthetic spectra using Equation 3 with $f_c = 30.0$ Hz, $\gamma = 2$,
 273 $n = 2.0$, and an arbitrary low-frequency amplitude level of $\Omega_0 = 10$. The attenuation
 274 parameter κ for each subarray is formulated as:

$$\kappa = \kappa_{path} + \kappa_{site}, \quad (8)$$

$$= \frac{tt - \sum_{i=0}^{i=N} tt_i}{Q_{path}} + \frac{\sum_{i=0}^{i=N} tt_i}{Q_{site}}. \quad (9)$$

275 The first term (κ_{path}) and the second term (κ_{site}) are the path and the site dependent
 276 attenuation. $\sum_{i=0}^{i=N} tt_i$ is the sum of travel time spent in the top $H = 400$ m, and tt is the
 277 total travel time from the source to the middle of the subarray. In our configuration,
 278 the waves spend less than 20% of time in the top 400 m. Q_{site} and Q_{path} are the site-
 279 and path-specific Q values. We calculate the ray travel time using Pykonal (using the
 280 Cartesian grid; [White et al., 2020](#)). The velocity structure is from [Chang et al. \(2024\)](#)
 281 for the top 1.5 km and [Rubinstein et al. \(2018\)](#) for below 1.5 km, and we assume $V_p =$
 282 $1.78V_s$. We generate synthetic spectra using either P-wave velocity or S-wave velocity
 283 using $Q_{site} = Q_s$ obtained from kappa of regional earthquakes.

284 We assume $Q_{path} = 1000$, which is a rough assumption that is chosen between [Singh](#)
 285 and [Herrmann \(1983\)](#) ($Q \approx 850$) and [Benz et al. \(1997\)](#) ($Q \approx 1300$) for this region. We
 286 also try $Q_{path} = 300$ ([Levandowski et al., 2021](#)) and find the results would not change
 287 because these values are all relatively high compared to Q_{site} . Note that the usage of a
 288 single Q_{path} without a source-depth dependence can be an over-simplification for real
 289 earthquakes, but we will focus on the difference in sites and will not address potential

TABLE 1 : Fitting conditions of KN20 and the synthetic tests. The synthetic spectra are generated using either P-wave velocity (V_p) or S-wave velocity ($V_s = V_p/1.78$) and a true $f_c = 30$ Hz. V_p and V_s are known parameters in the fitting. Test 1 is a benchmark that uses the same attenuation model to fit the spectra. Tests 2 – 5 use a model without the site term ($\kappa_{site} = 0$). Apparent f_c is the median of good measurements (<5% uncertainty) in the test.

Name	V_p or V_s	Attenuation model	Fixed variables	Dependent variables	$\frac{\text{Apparent } f_c}{\text{True } f_c}$
KN20	V_p	$\kappa = \kappa_{path}$	$Q_{total} = 600, n = 3.5$ (best fit)	$Q_{total}, n, \gamma, f_c$?
Synthetic test 1	V_p	$\kappa = \kappa_{path} + \kappa_{site}$	$Q_{path} = 350, n = 2.0$ (best fit)	$Q_{path}, Q_{site}, n, f_c$	100%
Synthetic test 2	V_p	$\kappa = \kappa_{path}$	$Q_{total} = 260, n = 2.0$ (best fit)	Q_{total}, n, f_c	96%
Synthetic test 3	V_p	$\kappa = \kappa_{path}$	$Q_{total} = 600, n = 3.5$	f_c	93%
Synthetic test 4	V_s	$\kappa = \kappa_{path}$	$Q_{total} = 280, n = 2.5$ (best fit)	Q_{total}, n, f_c	93%
Synthetic test 5	V_s	$\kappa = \kappa_{path}$	$Q_{total} = 600, n = 3.5$	f_c	68%

issues due to difference in Q_{path} here as the earthquakes are all relatively shallow (1.5 km – 5.5 km; see Discussions).

We fit the synthetic spectra with different attenuation models and source constraints (Table 1) in a series of tests to explore the trade-offs between source and path parameters. The travel times are known parameters from ray tracing and the velocity model (either V_p or V_s). Synthetic test 1 is a benchmark that includes the parameters used to generate the original synthetics (Equations 3 and 9). We allow both f_c and Q_{site} to vary and fix $\gamma = 2$. We perform a grid search to find the combination of Q_{path} and n that gives the overall best fit for all subarrays. We successfully recover $f_c = 30.0$ Hz and Q_{site} at all subarrays for these ideal spectra.

In synthetic tests 2 – 5, we ignore site effects with different source constraints (Table 1) when fitting the synthetic spectra (generated including the site term). We ignore the site term by assuming $\kappa_{site} = 0$ in Equation 9 and so the path Q equals to the total Q along the path of propagation: $Q_{path} = Q_{total}$. In test 2, we allow Q_{total} , n , and f_c to vary. A grid search finds a combination of $Q_{total} = 260$ and $n = 2.0$ gives the overall best fit (red star in Figure 8). This solution does not change if we use only Permian (higher Q_{site}) or Quaternary sites (lower Q_{site}). The map of residuals shows the trade-off between Q_{total} and n as spectral falloff parameter n tries to compensate for the

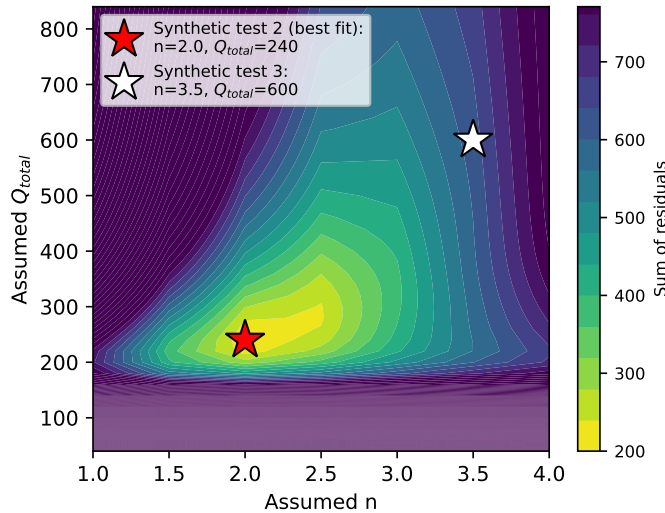


Figure 8: Trade-offs between attenuation and source spectral falloff parameter n when we attempt to use only travel-time dependent attenuation ($\kappa = \kappa_{path} = \text{travel time}/Q_{total}$) to fit synthetic spectra that include site attenuation ($\kappa = \kappa_{path} + \kappa_{site}$). Q_{total} is the overall Quality Factor assumed to characterize the attenuation. The colors indicate the sum of residuals from fitting the synthetic spectra at all subarrays. We perform synthetic test 2 using the overall best fit at the red star and test 3 using the combination at the white star (the best fit for real data in KN20).

308 unmodeled attenuation in the spectra. In test 3, we assume a combination of higher
 309 $Q_{total} = 600$ and higher $n = 3.5$ (white star in Figure 8), which is the best combination
 310 found for the actual data of event L1 in KN20, and solve for f_c .

311 Figure 9 shows the spectral fitting examples in the second and the third synthetic tests
 312 where we ignore the site terms. The models seem to fit well with small uncertainties.
 313 However, the measured f_c is significantly off from the true $f_c = 30$ Hz. Note that with
 314 some narrow-band amplification (such as the small peaks between 10 and 20 Hz seen
 315 in the observed spectra shown in Figure 2a), the grid-search might find $Q_{total} = 600$
 316 and $n = 3.5$ in Figure 9b to fit the spectra better.

317 Figure 10 shows the highly variable f_c measurements of all subarrays obtained in
 318 the sequence of synthetic tests (Table 1). These measurements have fairly good fits
 319 with uncertainty less than 5%. However, the apparent f_c scatter across 15 – 90 Hz
 320 among subarrays is due to the oversimplified attenuation model. Because the actual
 321 attenuation involves both the site Quality Factor (Q_{site}) and travel time (Equation 9),

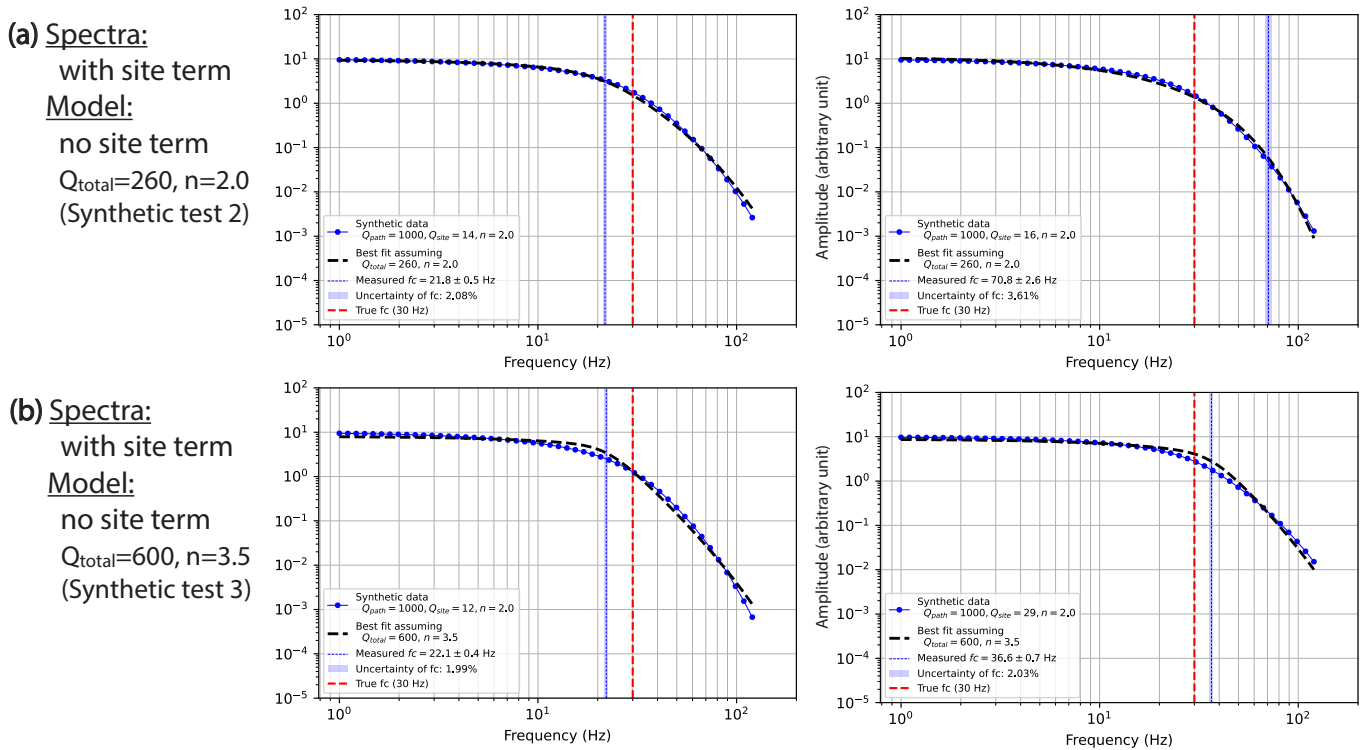


Figure 9: Models with different attenuation assumptions fit the synthetic spectra well while the corner frequency estimates are off. Synthetic tests 2 (a) and 3 (b) use models (black dashed curves) without site attenuation ($\kappa = \kappa_{\text{path}}$) to fit synthetics (blue curves) generated including site attenuation ($\kappa = \kappa_{\text{path}} + \kappa_{\text{site}}$). The apparent f_c (blue lines) can deviate significantly from the true $f_c = 30$ Hz (red lines) with small fitting uncertainties (blue shades).

the measured f_c correlates with the actual Q_{site} (i.e., Q_s) and the hypocentral distance.
 However, the large scattering can mask the correlations. When assuming another set of Q_{total} and n , the apparent relation between f_c and Q_s and the hypocentral distance changes (Figure 10b). The correlation between f_c and hypocentral distance may not be obvious.

Notice that the median f_c deviates from the true f_c . The deviation of the median f_c increases when the assumed n is higher than the true n (Figure 10b,c,d) because a varying n contributes to the parameter trade-off. The deviation of the median f_c can be severe with a low-velocity structure – in this case, V_s (Figure 10d), which is 1.78 times lower than V_p . This is because longer travel times increases the range of kappa

332 (Equation 4). Having a lower Q structure would have the same effect of increasing
333 kappa and increase the bias.

334 Now, we compare the real data of event L1 with the synthetic test results. KN20 used
335 a similar assumption to our third synthetic test. They assumed κ is entirely travel-time
336 dependent and found $Q_{total} = 600$ and $n = 3.5$ fit the overall data the best, possibly due
337 to site amplifications on the Quaternary sites. We observe similar site and distance
338 dependence in their f_c measurements comparing Figure 10(e) with 10b. The resem-
339 blance suggests trade-offs between f_c and Q_{site} , an overestimated n , and possibly a
340 biased f_c overall for this event due to site effects. Other local events also exhibit site
341 dependence (Figure S8, S9).

342 RE-DETERMINING SOURCE PARAMETERS CONSIDERING THE SITE ATTENUATION

343 We re-estimate the source parameters using P arrivals for all local events consider-
344 ing observed spectral decays. Different from the single-spectra approach in KN20 that
345 assumed $\kappa = \kappa_{path}$, we include site attenuation with $\kappa = \kappa_{path} + \kappa_{site}$. In addition, we
346 implement site-selection criteria to include only Permian sites with a higher apparent
347 Q_s or Q_p (from the regional events).

348 In the first test (refit test 1; Table 2), we let the site-dependent Q_{site} flexible in the
349 spectral fitting. We

- 350 1. Determine f_c and Q_{site} by fitting stack P-wave spectra (Equation 3) while fixing $\gamma = 2$
351 and $n = 2.0$.
- 352 2. Determine Q_{path} by grid-searching the Q_{path} that gives a lowest misfit in 1. for event
353 L1 (the most recorded event). We find $Q_{path} = 300$, which is applied to all other
354 events.

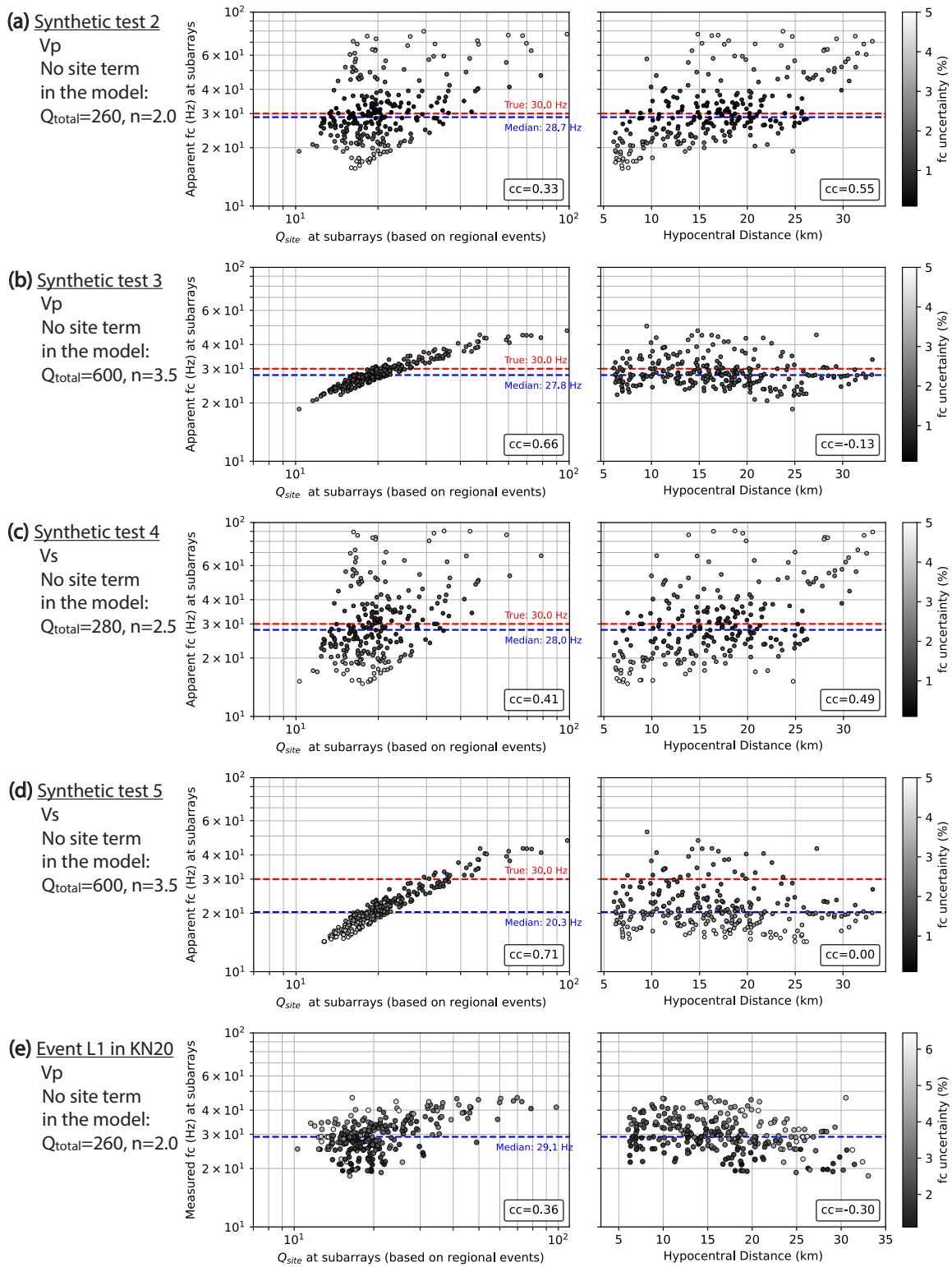


Figure 10: Relationship between apparent corner frequency (f_c) estimated ignoring site attenuation and the actual site attenuation (Q_s , left) and hypocentral distance (right). Synthetic tests 2 – 5 (a – d) assume $\kappa = \kappa_{path}$ with travel-time dependent attenuation to fit the synthetic spectra generated including site attenuation ($\kappa = \kappa_{path} + \kappa_{site}$). The median of the apparent f_c (blue dashed lines) deviate from the true f_c (30 Hz, red dashed lines). The deviation can be severe when κ increases (e.g., with lower S-wave velocity like in (d), or equivalently, with lower Q) and the source constraint n join the trade offs ($n = 3.5$, larger than the true value of 2). (e) is the measured f_c from actual data of event L1 in KN20. The gray scales indicate fitting uncertainty ((standard deviation of f_c)/ f_c x 100%). cc is Pearson's cross-correlation coefficient (all non-zero cc have p-values < 5%).

TABLE 2 : Fitting conditions for determining source parameters of LASSO local events. The refit tests 1 and 2 include an additional site term (κ_{site}) compared to KN20 that assumed a travel-time dependent attenuation. In the column of the dependent variables, n , γ , f_c , and Q_{site} are determined by fitting stack spectra, and Q_{total} and Q_{path} are determined by grid searching for the lowest misfit.

Name	Attenuation model	Site selection criteria	Fixed variables	Dependent variables
KN20	$\kappa = \kappa_{path}$	Permian + Quaternary sites	-	$Q_{total}, n, \gamma, f_c$
Refit test 1	$\kappa = \kappa_{path} + \kappa_{site}$	Permian sites with $Q_s > 37$	$n = 2.0, \gamma = 2$	Q_{path}, f_c, Q_{site}
Refit test 2	$\kappa = \kappa_{path} + \kappa_{site}$	Permian sites with $Q_p > 9$	$n = 2.0, \gamma = 2, Q_{site} = Q_p$	Q_{path}, f_c

355 Refit test 1 uses only Permian sites with Q_s higher than the 92th percentile ($Q_s > 37$).
 356 The travel times spent in the top 0.4 km (associated with Q_{site}) and below (associated
 357 with Q_{path}) are calculated using the Eikonal equations (White et al., 2020). The $Q_{path} =$
 358 300 we obtain is consistent with Levandowski et al. (2021) ($Q \approx 250$) but lower than
 359 $Q \approx 850$ in Singh and Herrmann (1983) for northern Oklahoma and $Q \approx 1300$ in Benz
 360 et al. (1997) for the CEUS. Our Q_{path} should be higher than their Q because Q_{path}
 361 already excluded Q_{site} . We use a 0.8 s window around the P arrivals to calculate the
 362 displacement spectra. Data treatment before spectral fitting includes applying point-
 363 wise quality control to discard data points with SNR less than 9, resampling the spectra
 364 into a constant interval on the log-frequency scale, and stacking the resampled spectra
 365 in each subarray. See Text S2 for details.

366 Figure 11 shows the re-calculated f_c for event L1 in refit test 1. We plot the f_c results
 367 with fitting uncertainty less than 100%. There is no correlation between f_c and Q_{site} or
 368 f_c and hypocentral distance in Figure 11 compared to the results in KN20 (Figure 10e).
 369 Although there might still be correlations (Figures S8 and S9) as the models are still
 370 simplified. Despite the large fitting uncertainty, the f_c among subarrays are consistent
 371 with a higher median f_c (41.2 Hz) than that in KN20 (29.1 Hz).

372 We further refine the results in refit test 1 by requiring a minimum fitting uncertainty
 373 for f_c to be less than 20%. Figure 12 shows the Q_{site} fitting results, taking the median

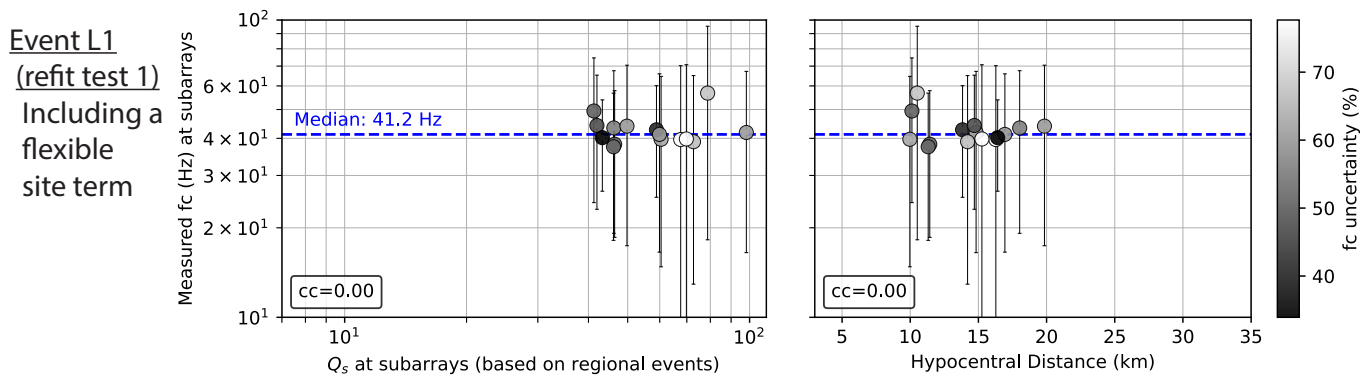


Figure 11: Correlation between corner frequency (f_c) and the actual Q_{site} (i.e., Q_s ; left) and hypocentral distance (right) decreases after including a flexible site term for event L1 in refit test 1. The gray scales indicate fitting uncertainty (standard deviation of f_c)/ $f_c \times 100\%$). The error bars indicate the standard deviation. The blue dashed lines are the median f_c . Each point represents a subarray with 15 – 20 stations within a 2.5 km diameter circle. cc is Pearson's cross-correlation coefficient (all non-zero cc have p -values < 5%). Compared to Figure 10e, the site- and distance-dependent correlations are removed in refit test 1 with a higher median f_c for event L1.

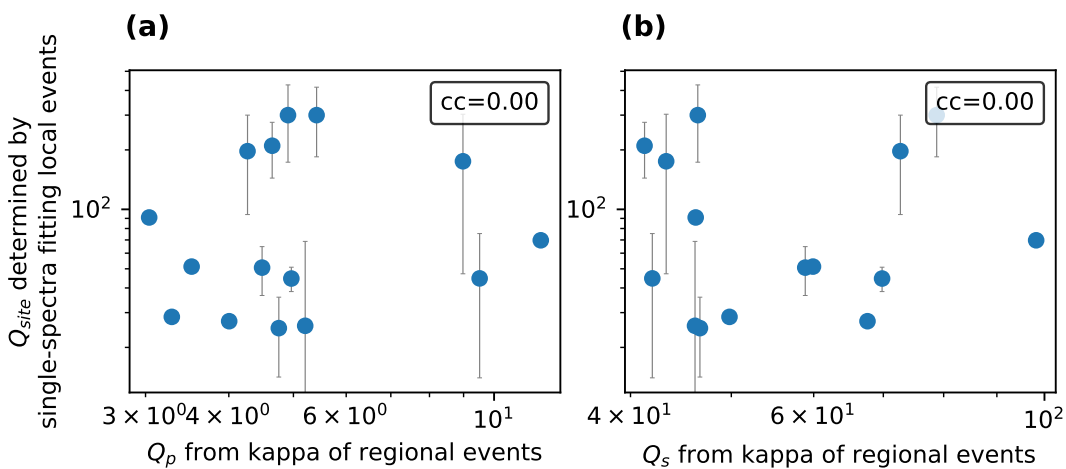


Figure 12: Site-dependent Quality Factor (Q_{site}) determined by spectral fitting local events (refit test 1) versus (a) Q_p and (b) Q_s determined from the kappa measured from the acceleration spectra of regional events. Q_{site} is the median of results from all local events with error bars indicating the standard deviation. Q_{site} are generally much lower than $Q_{path} = 300$. cc is Pearson's cross-correlation coefficient. The lack of correlations indicates that source spectra fitting of local events might not have good resolution for the spatial distribution of Q_{site} .

374 among available local events. The spectral fitting yields varying Q_{site} with many of them
 375 much lower than Q_{path} (300). However, the Q_{site} determined by spectral fitting does not
 376 correlate with Q_p and Q_s determined by kappa measured from the large distant events.
 377 The lack of correlation suggest that we do not have good resolution to determine the
 378 spatial distribution of Q_{site} in the source spectra fitting for local events.

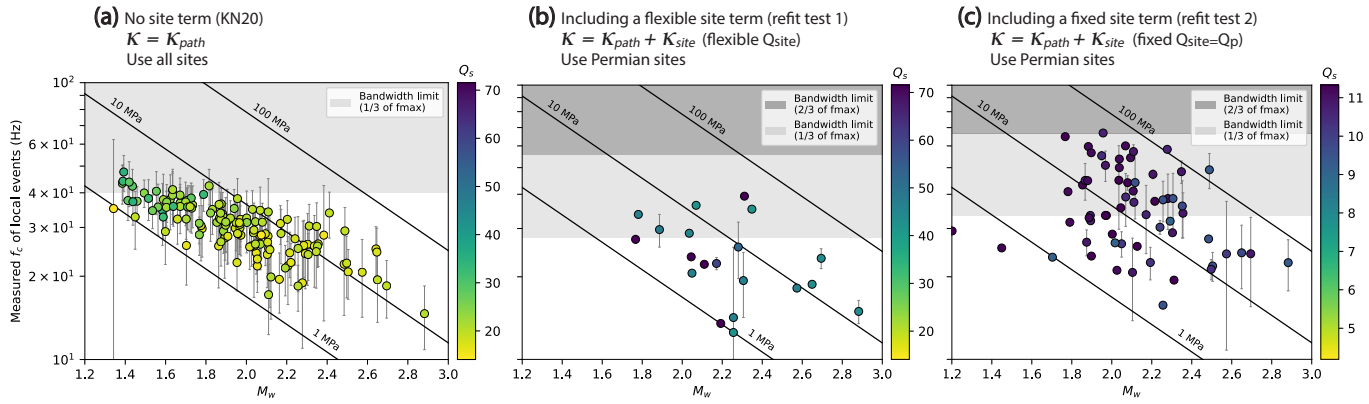


Figure 13: Apparent scaling relation between corner frequency (f_c) and moment magnitude (M_w) when (a) not including the site term (KN20), (b) including a flexible site term (refit test 1), and (c) including a fixed site term (refit test 2). Each dot is the median of an event (among subarrays) with error bars indicating the standard deviation of f_c . The colors indicate the average site attenuation (Q_s from regional events) of subarrays that participate in the measurements. The black lines are constant stress drops at 1, 10, and 100 MPa. The shades indicate approximate upper bandwidth limits defined as one and two-thirds of the maximum available frequency of the stacked spectra at subarrays.

379 Although we might not have good resolution to resolve Q_{site} in source spectra fitting,
 380 by including Q_{site} , we can reduce the biases that come from parameter trade-offs. We
 381 compare the source parameter scaling relation of refit test 1 with KN20. We calculate
 382 the stress drop using Equation 2, assuming β based on source depth and the velocity
 383 structure (Rubinstein et al., 2018), the same $k = 0.38$, and the same seismic moment
 384 (M_0) in KN20, and the moment magnitude (M_w) based on Hanks and Kanamori (1979).
 385 The single-spectra results in KN20 show smaller events deviating from the lines of con-
 386 stant stress drops (Figure 13a), whereas the results in refit test 1 do not exhibit obvious
 387 scaling relations (Figure 13b). The apparent scaling relation in KN20 is likely associ-
 388 ated with site effects, where small events typically with higher corner frequency are
 389 more susceptible to attenuation-related trade-offs. Furthermore, the colors in Figure
 390 13a show that smaller events have higher median Q_s , because small events are more
 391 likely being ignored by sites with a lower Q . This can cause another selection bias.

392 We conduct a second test (refit test 2; Table 2) that assumes Q_{site} is Q_p determined by
 393 the acceleration spectra of regional events. Here is how we determine the parameters:

³⁹⁴ 1. Determine f_c by fitting stack P-wave spectra (Equation 3) while fixing $\gamma = 2$, $n = 2.0$,
³⁹⁵ and $Q_{site} = Q_p$ (from the regional events).

³⁹⁶ 2. Determine Q_{path} by grid-searching the Q_{path} that gives a lowest misfit in 1. for event
³⁹⁷ L1 (the most recorded event). We find Q_{path} to be very large and use $Q_{path} = 99999$
³⁹⁸ for all events.

³⁹⁹ Refit test 2 uses only Permian sites with Q_p higher than the 92th percentile ($Q_p > 9$). We
⁴⁰⁰ require an uncertainty of f_c to be less than 20% and calculate the moment magnitudes
⁴⁰¹ and stress drops (Figure 13c). The number of results increases compared to the first test

⁴⁰² because fixing Q_{site} reduces the degree of freedom which reduces the uncertainty. The
⁴⁰³ source parameters still do not exhibit an obvious scaling relation in the second test.

⁴⁰⁴ The stress drops (median $\Delta\sigma = 18$ MPa) are in general higher than KN20 (5.0 MPa)
⁴⁰⁵ and refit test 1 (6.7 MPa). This suggests possibly higher actual stress drops. Or, this can
⁴⁰⁶ also result from higher P-wave spectral decays for large distant events (where our Q_p
⁴⁰⁷ estimates are from) than those for the small local events (the actual Q_p), which causes
⁴⁰⁸ higher apparent corner frequencies.

⁴⁰⁹ DISCUSSIONS

⁴¹⁰ Highly attenuating shallow layers with large site-dependence

⁴¹¹ The acceleration spectra of regional earthquakes reveal that attenuation is highly site-
⁴¹² dependent and mainly occurs at the near surface. Despite that the earthquakes are
⁴¹³ more than 125 km away, 10% to 75% of the total kappa is site-related for S waves and
⁴¹⁴ can be more than 90% for P waves. Abercrombie (1997) found that 90% of attenuation
⁴¹⁵ happens in the top 3 km for earthquakes within 15 km at Cajon Pass, California. Our
⁴¹⁶ earthquakes are nine more times away and the site attenuation can still dominate. The

417 surface Quaternary sediments tend to have higher spectral decays, but the Permian
418 rocks can have a high spectral decay as well (Figure 5).

419 We find $Q_p = 3 - 25$ (mainly on the Permian sites) and $Q_s = 10 - 100$ (on both
420 Quaternary and Permian sites) in the upper 400 m, and $Q_p = 10 - 80$ and $Q_s = 40 - 240$
421 in the upper 2 km (Figure 7). The Q values are approximately within the same range
422 of previous borehole studies in California (Jongmans and Malin, 1995; Abercrombie,
423 1999) and Switzerland (Bethmann et al., 2012). In comparison, the Q of the deep struc-
424 ture (derived from our regional events with hypocenter located at 4 – 6 km depth,
425 125 km away) is much higher ($Q > 3000$). These observations are consistent with the
426 tectonic and geological environment. The Central US is in the intra-plate stable tec-
427 tonic regime with soft sediments overlying stiff formations (Johnson and Luza, 2008).
428 Young alluviums deposited on the post-glacier land, creating local large site effect with
429 a flat topography. Our results can likely extend to much of the Central US with similar
430 geological conditions.

431 Both the site spectral decay and Q values indicate higher attenuation for P waves than
432 for S waves. Bethmann et al. (2012) also found $Q_p/Q_s \leq 1$ in Switzerland, whereas the
433 California studies (Jongmans and Malin, 1995; Abercrombie, 1999) have $Q_p/Q_s \geq 1$.
434 Variations in Q_p/Q_s can be affected by water contents. Partial saturation tends to have
435 $Q_p/Q_s < 1$ while complete saturation tends to have $Q_p/Q_s > 1$ (Winkler and Nur, 1982;
436 Clouser and Langston, 1991; Parolai et al., 2022). We do not further investigate the
437 difference between Q_p and Q_s in this study.

438 There are some limitations on the Q values derived from kappa in this study. First, our
439 Q_p and Q_s are lower bound because the shallow velocity is likely lower. The 3D velocity

model we used to derive Q lacks good resolution in the upper 50 m. Local average shear-wave velocity in the top 30 m (V_{s30}) is about 400 m/s (Zalachor et al., 2017), which is much lower than the $V_s > 900$ m/s at 50 m depth in our velocity model (Figure S5). The potentially underestimated travel times and Q are less than 5% (for $H \geq 400$ m; Equation 7). Second, we do not consider potential broadband amplification (e.g., Boore and Joyner, 1997; Campbell and Bozorgnia, 2014), the apparent Q might be higher at stiff sites and lower at soft sites than the actual values. The apparent Q is sufficient for our purpose of understanding potential site effects for source parameter estimation.

448 Implications of shallow attenuation on spectral fitting

Under this attenuation structure, assuming a dominantly travel-time-dependent attenuation in Brune's model would cause the apparent corner frequency to vary from site to site and bias overall measurements. The spectral fitting appears good but the f_c deviates from the true value (Figure 9). The f_c correlates with site attenuation with large scattering from one subarray to another (Figure 6b,10). Some studies used the relation between f_c and hypocentral distance to examine uncorrected attenuation (e.g., Figure 13 in Bindi et al., 2020). However, the apparent relation between f_c and distances can be unobvious depending on model assumptions (Figures 10). A lack of correlation between f_c and distance (or travel time) does not suggest little influence of site effects. The apparent n values tend to be larger to compensate for the unmodeled site attenuation as both are independent of the total travel time.

460 Methods to reduce site-effect-related bias and uncertainty

We demonstrate that by adding a site-attenuation term (κ_{site}), restricting spectral fitting to sites on stiffer formations (Permian rocks with higher Q), and implementing

the source constraint (fixing n), we can significantly reduce the apparent scaling relation (Figure 13). The spectral-ratio approach is also effective in removing the site effects. Source parameters estimated using the spectral-ratio approach do not exhibit an apparent scaling relation (Kemna et al., 2020) or correlations with site conditions (Chang et al., 2023). However, the spectral-ratio methods involve other uncertainties (Abercrombie, 2015), and the limited EGF availability for small events can introduce other selection biases. We also attempted to derive non-parametric site response spectra for correction using regional earthquakes. However, because the regional earthquakes have limited SNR above 30 Hz due to attenuation (Figure S10), we could not get reliable f_c measurements from the corrected spectra.

Chang et al. (2023) attempted to correct site effects in the source parameter measurements by removing a linear trend between site amplification and f_c and M_0 . However, their trend removal is based on the median of station-wise measurements in individual events. Such median-based correction underestimates the event-wise bias due to site effects, because the median can deviate from the true value (Figure 10). On the other hand, one might attempt to find a site-specific scaling factor to correct f_c . However, because the scattering and biases not only relate to the site condition (Q_{site}) but also to the source-station configuration, and the fitting assumptions, finding a site-specific correction is impossible. Depending on the fitting assumptions, the apparent f_c can have different apparent relations with site conditions and distance. Once the measurements are made, correcting the measurements is not easier than re-doing the fitting under a more adequate assumption.

485 Potential impacts of site amplification

486 We use the site-dependent spectral decay ($\kappa_{0,acc}$) from large events to estimate that of
487 local small events. The spectral decay parameter could contain both attenuation and
488 broadband amplification (Boore and Joyner, 1997). We do avoid local strong resonance
489 by averaging spectra and measuring using wide (> 15 Hz) and carefully selected fre-
490 quency bands (Figure 2). Still, sites on the Quaternary formations tend to have elevated
491 amplitudes under 25 Hz (Figure S10). Hence, the Q_p and Q_s estimated from the spec-
492 tral decay are apparent values. In refit test 2, assuming the same Q_p estimated from
493 large regional events for the small local events yields generally higher corner frequen-
494 cies and stress drops compared to refit test 1. The stress drops are still within the range
495 that agrees with previous studies (Huang et al., 2017). However, the apparent higher f_c
496 might indicate that the observed spectra of small local events have higher apparent Q_p
497 compared to the large regional events, possibly due to less broadband amplification at
498 lower frequencies for the small local events, if other parameters (e.g., n) are the same
499 for these earthquakes.

500 Although we try to minimize the impact of local strong resonances, a consistent
501 small amplitude bulge can still affect the single-spectral fitting given how close a false
502 model with a biased f_c can resemble the spectra (Figure 9). Chang et al. (2023) found
503 that ground motions of regional events correlates with f_c in KN20. The advantage of
504 spectral-ratio methods, if available, is to take care of the general site and path effects.
505 Otherwise, the site and path effects need to be carefully considered. The unmodeled
506 amplification might cause a higher apparent spectral fall-off rate (n), which if used,
507 would participate in the trade-off and result in large biases in f_c (Figure 10).

508 Other potential factors

509 There is a simplification in our attenuation model, which is the usage of a single path-
510 dependent attenuation Q_{path} in Equation 9. In reality, because of the Earth's layered
511 structure, for two earthquakes with the same hypocentral distance, the one directly
512 beneath the station, and thus at a deeper depth, can experience very different attenu-
513 ation compared to the one at shallower depth. Using the same Q_{path} to characterize
514 both earthquakes causes an apparent scaling relation with increasing source depth
515 ([Abercrombie et al., 2021](#)). [Baltay et al. \(2024\)](#) observed that stress drops estimated
516 without considering source-depth dependent attenuation exhibit a stronger correla-
517 tion with source depths, in which attenuation likely plays a role. In this study, the
518 depths of local earthquakes are all relatively shallow (1.5 km – 5.5 km), and the ray
519 paths to most of the stations spend significant times traveling in nearly horizontal lay-
520 ers; hence, a purely travel-time dependent Q_{path} may be sufficient. However, we note
521 that a depth-dependent Q_{path} is required when analyzing earthquakes with greater
522 depths.

523 Another source of uncertainty come from source complexity. Some studies observed
524 evidence of complicated source ruptures for microearthquakes at LASSO ([Trugman](#)
525 [et al., 2021](#); [Pennington et al., 2022](#); [Chang et al., 2023](#)). Fitting complex source spec-
526 tra with a simple Brune's or a spectral-ratio model might also introduce misfit-related
527 uncertainties.

528 CONCLUSION

529 We measure the high-frequency spectral decay parameter kappa (κ_{acc}) using the
530 acceleration spectra of regional earthquakes ($M_L = 3.6 - 3.7$) to investigate shallow

531 attenuation at the LArge-n Seismic Survey in Oklahoma (LASSO). The dense surface
532 station coverage allows us to stack in multiple subarrays to improve the stability of the
533 measurements while maintain a high spatial resolution. 10% – 75% of the total kappa
534 is site-dependent for S waves and can be more than 90% for P waves, even for events
535 that are over 125 km away. The range of site-related kappa is much larger than the total
536 path-related kappa across the 25 km x 32 km area of the array.

537 We derived the apparent Quality Factor (Q) for P and S waves using kappa. The Q
538 values decrease rapidly at shallower depths. In the top 2 km, Q_s ranges from 30 to 224,
539 and in the top 400 m, Q_s ranges from 10 to 80. The Quaternary sediments tend to have
540 higher attenuation (most have $Q_s < 30$ in the top 400 m) but the Permian rocks can
541 be highly attenuating as well. Most Q_p in the top 400 m are lower than 10. The cor-
542 ner frequency (f_c) estimated using the single-spectra approach in [Kemna et al. \(2020\)](#)
543 (denoted as KN20) negatively correlates with the site-dependent kappa, suggesting
544 influences of site effects.

545 We investigate the impact of ignoring site-dependent spectral decay when fitting with
546 Brune's source model for local microearthquakes ($1.3 < M_w < 3.0$). Using synthetic
547 spectra, we demonstrate that mixing stations with different site conditions while ignor-
548 ing site-specific attenuation results in large inter-station variation in apparent f_c and
549 serious biases between events (Figure 10). The impact is more severe if the range of
550 site-dependent kappa increases, such as in lower velocity structures or with higher
551 site-dependent attenuations. The spectral fall-off parameter n tends to be higher than
552 the actual value to accommodate the site-dependent attenuation, which then worsens
553 the trade-offs and can cause serious bias in f_c (Figure 10e). The biased measurements

554 may have little or no apparent correlation with distance depending on fitting assump-
555 tions. The fitting uncertainty also fails to account for the scattering and bias because
556 of the non-uniqueness of the model (Figure 9).

557 By adding a site-dependent attenuation term, using only sites on stiff formations, and
558 fixing n , we can largely remove the apparent scaling relation between earthquake size
559 and dimension in the single-spectra fitting results in KN20. This study demonstrates
560 the importance of considering near-surface attenuation even within a simple, flat small
561 region. Using a small number of stations with controlled site conditions is more precise
562 and accurate than having a large number of stations with uncontrolled site conditions.

563 DATA AND RESOURCES

564 We use ObsPy ([Beyreuther et al., 2010](#)) for earthquake data processing. We use the
565 TauP module in Obspy to calculate travel times for regional events. All spectral fit-
566 tings in Section and are done using LMFIT ([Newville et al., 2016](#)). We use PyKonal
567 ([White et al., 2020](#)) to calculate travel times for all local events. All data used in this
568 paper came from published sources listed in the references. The supplemental doc-
569 ument provides additional supporting information including a detailed description
570 of data processing, supplemental figures, and tables with detailed information of the
571 earthquakes analyzed.

572 DECLARATION OF COMPETING INTERESTS

573 The authors acknowledge there are no conflicts of interest recorded.

574 **ACKNOWLEDGMENTS**

575 We thank Annemarie Baltay, Gail Atkinson, and an anonymous reviewer for providing
576 constructive feedbacks that significantly improve the manuscript. This research
577 was supported by the U.S. Geological Survey under Grant G20AP00022, G20AP00023,
578 G22AP00012, and G22AP00035 to Massachusetts Institute of Technology and Boston
579 University. Nori Nakata is partially supported by the U.S. Department of Energy under
580 Award Number DE-AC02-05CH11231 for this study.

581 **REFERENCES**

- 582 Abercrombie, R. and P. Leary (1993). Source parameters of small earthquakes recorded at 2.5 km depth, Cajon Pass, southern California:
583 Implications for earthquake scaling. *Geophysical Research Letters* **20**(14), 1511–1514.
- 584 Abercrombie, R. E. (1995). Earthquake source scaling relationships from 1 to 5 M_L using seismograms recorded at 2.5 km depth. *Journal*
585 *of Geophysical Research: Solid Earth* **100**(B12), 24015–24036.
- 586 Abercrombie, R. E. (1997). Near-surface attenuation and site effects from comparison of surface and deep borehole recordings. *Bulletin of*
587 *the Seismological Society of America* **87**(3), 731–744.
- 588 Abercrombie, R. E. (1999). A summary of attenuation measurements from borehole recordings of earthquakes: The 10 hz transition
589 problem. *Q of the Earth: Global, Regional, and Laboratory Studies*, 475–487.
- 590 Abercrombie, R. E. (2015). Investigating uncertainties in empirical Green's function analysis of earthquake source parameters. *Journal of*
591 *Geophysical Research: Solid Earth* **120**(6), 4263–4277.
- 592 Abercrombie, R. E. (2021). Resolution and uncertainties in estimates of earthquake stress drop and energy release. *Philosophical*
593 *Transactions of the Royal Society A* **379**(2196), 20200131.
- 594 Abercrombie, R. E., A. Baltay, S. Chu, T. Taira, D. Bindi, O. Boyd, X. Chen, E. Cochran, E. Devin, D. Dreger, W. Ellsworth, W. Fan,
595 R. Harrington, Y. Huang, K. Kemna, M. Liu, A. Oth, G. Parker, C. Pennington, M. Picozzi, C. Ruhl, P. M. Shearer, D. Spallarossa,
596 D. T. Trugman, I. Vandevert, Q. Wu, C. Yoon, E. Yu, G. Beroza, T. Eulenfeld, T. Knudsen, K. Mayeda, P. Morasca, J. Neely, J. Roman-
597 Nieves, C. Satriano, M. Supino, W. Walter, R. Archuleta, G. Atkinson, G. Calderoni, C. Ji, H. Yang, and J. Zhang (2024). Overview of The
598 SCEC/USGS Community Stress Drop Validation Study using the 2019 Ridgecrest earthquake sequence. *Bulletin of the Seismological*
599 *Society of America*.
- 600 Abercrombie, R. E., S. Bannister, J. Ristau, and D. Doser (2016). Variability of earthquake stress drop in a subduction setting, the Hikurangi
601 Margin, New Zealand. *Geophysical Journal International*, ggw393.
- 602 Abercrombie, R. E., D. T. Trugman, P. M. Shearer, X. Chen, J. Zhang, C. N. Pennington, J. L. Hardebeck, T. H. Goebel, and C. J. Ruhl (2021).
603 Does earthquake stress drop increase with depth in the crust? *Journal of Geophysical Research: Solid Earth* **126**(10), e2021JB022314.

- 604 Allmann, B. P. and P. M. Shearer (2009). Global variations of stress drop for moderate to large earthquakes. *Journal of Geophysical Research: Solid Earth* **114**(B1).
- 605 Anderson, J. G. (1986). Implication of attenuation for studies of the earthquake source. *Earthquake Source Mechanics* **37**, 311–318.
- 606 Anderson, J. G. and S. E. Hough (1984). A model for the shape of the Fourier amplitude spectrum of acceleration at high frequencies. *Bulletin of the Seismological Society of America* **74**(5), 1969–1993.
- 607 Andrews, D. (1986). Objective determination of source parameters and similarity of earthquakes of different size. *Earthquake source mechanics* **37**, 259–267.
- 608 Atkinson, G. M. and I. Beresnev (1997). Don't call it stress drop. *Seismological Research Letters* **68**(1), 3–4.
- 609 Baltay, A., R. Abercrombie, S. Chu, and T. Taira (2024). The SCEC/USGS Community Stress Drop Validation Study Using the 2019 Ridgecrest Earthquake Sequence. *Seismica* **3**(1).
- 610 Benz, H. M., A. Frankel, and D. M. Boore (1997). Regional Lg attenuation for the continental United States. *Bulletin of the Seismological Society of America* **87**(3), 606–619.
- 611 Bethmann, F., N. Deichmann, and P. M. Mai (2012). Seismic wave attenuation from borehole and surface records in the top 2.5 km beneath the city of Basel, Switzerland. *Geophysical Journal International* **190**(2), 1257–1270.
- 612 Beyreuther, M., R. Barsch, L. Krischer, T. Megies, Y. Behr, and J. Wassermann (2010). ObsPy: A Python toolbox for seismology [Software]. *Seismological Research Letters* **81**(3), 530–533.
- 613 Bindi, D., K. Mayeda, D. Spallarossa, M. Picozzi, A. Oth, P. Morasca, and W. R. Walter (2024, October). Numerical tests to evaluate the effect of constraining the spectral shape of reference events on source parameter scaling. *Bulletin of the Seismological Society of America*.
- 614 Bindi, D., D. Spallarossa, M. Picozzi, and P. Morasca (2020). Reliability of source parameters for small events in central Italy: Insights from spectral decomposition analysis applied to both synthetic and real data. *Bulletin of the Seismological Society of America* **110**(6), 3139–3157.
- 615 Bindi, D., D. Spallarossa, M. Picozzi, A. Oth, P. Morasca, and K. Mayeda (2023). The community stress-drop validation study—part II: Uncertainties of the source parameters and stress drop analysis. *Seismological Society of America* **94**(4), 1992–2002.
- 616 Boatwright, J. (1978). Detailed spectral analysis of two small new york state earthquakes. *Bulletin of the Seismological Society of America* **68**(4), 1117–1131.
- 617 Boatwright, J. (1980). A spectral theory for circular seismic sources; simple estimates of source dimension, dynamic stress drop, and radiated seismic energy. *Bulletin of the Seismological Society of America* **70**(1), 1–27.
- 618 Boore, D. (1986). The effect of finite bandwidth on seismic scaling relationships. *Earthquake Source Mechanics* **37**, 275–283.
- 619 Boore, D. M. and W. B. Joyner (1997). Site amplifications for generic rock sites. *Bulletin of the seismological society of America* **87**(2), 327–341.
- 620 Brune, J. N. (1970). Tectonic stress and the spectra of seismic shear waves from earthquakes. *Journal of geophysical research* **75**(26), 4997–5009.
- 621 Campbell, K. W. and Y. Bozorgnia (2014). NGA-West2 ground motion model for the average horizontal components of PGA, PGV, and 5% damped linear acceleration response spectra. *Earthquake Spectra* **30**(3), 1087–1115.

- 638 Castro, R., J. Anderson, and S. Singh (1990). Site response, attenuation and source spectra of S waves along the Guerrero, Mexico,
639 subduction zone. *Bulletin of the Seismological Society of America* **80**(6A), 1481–1503.
- 640 Catchings, R. (1999). Regional V_p, V_s, V_p/V_s, and Poisson's ratios across earthquake source zones from Memphis, Tennessee, to St. Louis,
641 Missouri. *Bulletin of the Seismological Society of America* **89**(6), 1591–1605.
- 642 Chang, H., R. E. Abercrombie, N. Nakata, C. N. Pennington, K. B. Kemna, E. S. Cochran, and R. M. Harrington (2023). Quantifying
643 site effects and their influence on earthquake source parameter estimations using a dense array in Oklahoma. *Journal of Geophysical
644 Research: Solid Earth*, e2023JB027144.
- 645 Chang, H., Q. H., Z. Zhang, N. Nakata, and R. Abercrombie (2024). Investigation of site amplifications using ambient-noise-derived shallow
646 velocity structures under a dense array in Oklahoma. Manuscript submitted for publication.
- 647 Clouser, R. H. and C. A. Langston (1991). Q_p-Q_s relations in a sedimentary basin using converted phases. *Bulletin of the Seismological
648 Society of America* **81**(3), 733–750.
- 649 Cocco, M., E. Tinti, and A. Cirella (2016). On the scale dependence of earthquake stress drop. *Journal of Seismology* **20**, 1151–1170.
- 650 Cochran, E. S., A. Wickham-Piotrowski, K. B. Kemna, R. M. Harrington, S. L. Dougherty, and A. F. Peña Castro (2020). Minimal clustering
651 of injection-induced earthquakes observed with a large-n seismic array. *Bulletin of the Seismological Society of America* **110**(5), 2005–
652 2017.
- 653 Crain, K. D. and J. C. Chang (2018). Elevation map of the top of the crystalline basement in Oklahoma and surrounding states. *Oklahoma
654 Geol. Surv. Open-File Rept. OF1-2018*.
- 655 Dougherty, S. L., E. S. Cochran, and R. M. Harrington (2019). The Large-N seismic survey in Oklahoma (LASSO) experiment. *Seismological
656 Research Letters* **90**(5), 2051–2057.
- 657 Eshelby, J. D. (1957). The determination of the elastic field of an ellipsoidal inclusion, and related problems. *Proceedings of the royal society
658 of London. Series A. Mathematical and physical sciences* **241**(1226), 376–396.
- 659 Hanks, T. C. and H. Kanamori (1979). A moment magnitude scale. *Journal of Geophysical Research: Solid Earth* **84**(B5), 2348–2350.
- 660 Hartzell, S. H. (1978). Earthquake aftershocks as Green's functions. *Geophysical Research Letters* **5**(1), 1–4.
- 661 Hartzell, S. H. (1992). Site response estimation from earthquake data. *Bulletin of the Seismological Society of America* **82**(6), 2308–2327.
- 662 Hauksson, E. and P. M. Shearer (2006). Attenuation models (Q_p and Q_s) in three dimensions of the southern California crust: Inferred
663 fluid saturation at seismogenic depths. *Journal of Geophysical Research: Solid Earth* **111**(B5).
- 664 Heran, W. D., G. N. Green, and D. B. Stoeser (2003). A digital geologic map database for the state of Oklahoma. Technical report, U.S.
665 Geological Survey, Denver, CO.
- 666 Hough, S. (1997). Empirical Green's function analysis: Taking the next step. *Journal of Geophysical Research: Solid Earth* **102**(B3), 5369–
667 5384.
- 668 Hough, S. and J. Anderson (1988). High-frequency spectra observed at Anza, California: implications for Q structure. *Bulletin of the
669 Seismological Society of America* **78**(2), 692–707.
- 670 Huang, Y., W. L. Ellsworth, and G. C. Beroza (2017). Stress drops of induced and tectonic earthquakes in the central United States are
671 indistinguishable. *Science advances* **3**(8), e1700772.

- 672 Ji, C., R. J. Archuleta, and Y. Wang (2022). Variability of spectral estimates of stress drop reconciled by radiated energy. *Bulletin of the*
673 *Seismological Society of America* **112**(4), 1871–1885.
- 674 Johnson, K. S. and K. V. Luza (2008). *Earth sciences and mineral resources of Oklahoma*. Oklahoma Geological Survey.
- 675 Jongmans, D. and P. E. Malin (1995). Microearthquake S-wave observations from 0 to 1 km in the Varian well at Parkfield, California.
676 *Bulletin of the Seismological Society of America* **85**(6), 1805–1820.
- 677 Kemna, K., A. Peña Castro, R. Harrington, and E. S. Cochran (2020). Using a large-n seismic array to explore the robustness of spectral
678 estimations. *Geophysical Research Letters* **47**(21), e2020GL089342.
- 679 Kemna, K. B., A. Verdecchia, and R. M. Harrington (2021). Spatio-temporal evolution of earthquake static stress drop values in the 2016–
680 2017 central Italy seismic sequence. *Journal of Geophysical Research: Solid Earth* **126**(11), e2021JB022566.
- 681 Ko, Y.-T., B.-Y. Kuo, and S.-H. Hung (2012). Robust determination of earthquake source parameters and mantle attenuation. *Journal of*
682 *Geophysical Research: Solid Earth* **117**(B4).
- 683 Ktenidou, O., N. Abrahamson, R. Darragh, and W. Silva (2016). A methodology for the estimation of kappa (κ) from large datasets, example
684 application to rock sites in the NGA-East database, and implications on design motions. *PEER Report 2016* **1**.
- 685 Ktenidou, O.-J., N. A. Abrahamson, S. Drouet, and F. Cotton (2015). Understanding the physics of kappa (κ): Insights from a downhole
686 array. *Geophysical Journal International* **203**(1), 678–691.
- 687 Levandowski, W., O. S. Boyd, D. AbdelHameid, and D. E. McNamara (2021). Crustal seismic attenuation of the central United States and
688 Intermountain West. *Journal of Geophysical Research: Solid Earth* **126**(12), e2021JB022097.
- 689 Madariaga, R. (1976). Dynamics of an expanding circular fault. *Bulletin of the Seismological Society of America* **66**(3), 639–666.
- 690 Mayeda, K., L. Malagnini, and W. R. Walter (2007). A new spectral ratio method using narrow band coda envelopes: Evidence for non-
691 self-similarity in the Hector Mine sequence. *Geophysical Research Letters* **34**(11).
- 692 Newville, M., T. Stensitzki, D. B. Allen, M. Rawlik, A. Ingargiola, and A. Nelson (2016). LMFIT: Non-linear least-square minimization and
693 curve-fitting for Python [Software]. *Astrophysics Source Code Library*, ascl-1606.
- 694 Nye, T., V. J. Sahakian, E. King, A. Baltay, and A. Klimasewski (2023). Estimates of κ_0 and effects on ground motions in the San Francisco
695 Bay Area. *Bulletin of the Seismological Society of America* **113**(2), 823–842.
- 696 Oth, A., D. Bindi, S. Parolai, and D. Di Giacomo (2011). Spectral analysis of K-NET and KiK-net data in Japan, Part II: On attenuation
697 characteristics, source spectra, and site response of borehole and surface stations. *Bulletin of the Seismological Society of America* **101**(2),
698 667–687.
- 699 Oth, A., H. Miyake, and D. Bindi (2017). On the relation of earthquake stress drop and ground motion variability. *Journal of Geophysical*
700 *Research: Solid Earth* **122**(7), 5474–5492.
- 701 Parolai, S., C. G. Lai, I. Dreossi, O.-J. Ktenidou, and A. Yong (2022). A review of near-surface Q_S estimation methods using active and
702 passive sources. *Journal of Seismology* **26**(4), 823–862.
- 703 PEER (2015). NGA-East: Median ground-motion models for the Central and Eastern North America region (No.2015/04). Technical
704 report, Pacific Earthquake Engineering Research Center (PEER).

- 705 Pennington, C. N., H. Chang, J. L. Rubinstein, R. E. Abercrombie, N. Nakata, T. Uchide, and E. S. Cochran (2022). Quantifying the
706 sensitivity of microearthquake slip inversions to station distribution using a dense nodal array. *Bulletin of the Seismological Society of*
707 *America* **112**(3), 1252–1270.
- 708 Prieto, G. A. (2022). The multitaper spectrum analysis package in Python. *Seismological Society of America* **93**(3), 1922–1929.
- 709 Rubinstein, J. L., W. L. Ellsworth, and S. L. Dougherty (2018). The 2013–2016 induced earthquakes in Harper and Sumner Counties,
710 southern Kansas. *Bulletin of the Seismological Society of America* **108**(2), 674–689.
- 711 Shearer, P. M. (2009). Surface waves and normal modes: Rayleigh waves. In *Introduction to seismology*, pp. 219–224. Cambridge university
712 press.
- 713 Shearer, P. M., R. E. Abercrombie, D. T. Trugman, and W. Wang (2019). Comparing EGF methods for estimating corner frequency and
714 stress drop from P wave spectra. *Journal of Geophysical Research: Solid Earth* **124**(4), 3966–3986.
- 715 Shearer, P. M., G. A. Prieto, and E. Hauksson (2006). Comprehensive analysis of earthquake source spectra in southern California. *Journal*
716 *of Geophysical Research: Solid Earth* **111**(B6).
- 717 Shearer, P. M., I. Vandevert, W. Fan, R. E. Abercrombie, D. Bindi, G. Calderoni, X. Chen, W. Ellsworth, R. Harrington, Y. Huang, T. Knudson,
718 M. Roßbach, C. Satriano, M. Supino, D. T. Trugman, and J. Zhang (2024). Earthquake source spectra estimates vary widely for two
719 Ridgecrest aftershocks because of differences in attenuation corrections. *Bulletin of the Seismological Society of America*.
- 720 Singh, S. and R. B. Herrmann (1983). Regionalization of crustal coda Q in the continental United States. *Journal of Geophysical Research:*
721 *Solid Earth* **88**(B1), 527–538.
- 722 Supino, M., G. Festa, and A. Zollo (2019). A probabilistic method for the estimation of earthquake source parameters from spectral
723 inversion: application to the 2016–2017 Central Italy seismic sequence. *Geophysical Journal International* **218**(2), 988–1007.
- 724 Toksöz, M., D. H. Johnston, and A. Timur (1979). Attenuation of seismic waves in dry and saturated rocks: I. Laboratory measurements.
725 *Geophysics* **44**(4), 681–690.
- 726 Trugman, D. T., S. X. Chu, and V. C. Tsai (2021). Earthquake source complexity controls the frequency dependence of near-source radiation
727 patterns. *Geophysical Research Letters* **48**(17), e2021GL095022.
- 728 U.S. Geological Survey. Earthquake Hazards Program Advanced National Seismic System (ANSS) Comprehensive Catalog of Earthquake
729 Events and Products: Catalog ($m > 3$) in Central Oklahoma (2016-04-14–2016-05-10) [data set]. Last accessed on 2022-09-19.
- 730 Van Houtte, C., S. Drouet, and F. Cotton (2011). Analysis of the origins of κ (kappa) to compute hard rock to rock adjustment factors for
731 GMPEs. *Bulletin of the Seismological Society of America* **101**(6), 2926–2941.
- 732 White, M. C., H. Fang, N. Nakata, and Y. Ben-Zion (2020). PyKonal: a Python package for solving the eikonal equation in spherical and
733 Cartesian coordinates using the fast marching method [Software]. *Seismological Research Letters* **91**(4), 2378–2389.
- 734 Winkler, K. W. and A. Nur (1982). Seismic attenuation: Effects of pore fluids and frictional-sliding. *Geophysics* **47**(1), 1–15.
- 735 Zalachor, G., E. M. Rathje, and J. G. Paine (2017). v_{S30} characterization of Texas, Oklahoma, and Kansas using the P-wave seismogram
736 method. *Earthquake Spectra* **33**(3), 943–961.

737 **FULL MAILING ADDRESS FOR EACH AUTHOR**

- 738 • Hilary Chang: Department of Earth, Atmospheric, and Planetary Sciences,
739 Massachusetts Institute of Technology; 54-216, 77 Massachusetts, Cambridge, MA,
740 02139, USA
- 741 • Rachel E. Abercrombie: Department of Earth and Environment, Boston Universiy;
742 685 Commonwealth Avenue, Room 130, Boston, MA, 02215, USA
- 743 • Nori Nakata: Earth and Environmental Sciences Area, Lawrence Berkeley National
744 Laboratory; 1 Cyclotron Rd, Berkeley, CA, 94720, USA

1 Regional and local earthquakes recorded at the LASSO array and the
746 variability of source parameter measurements using a single-spectra fit-
747 ting approach. In **(a)**, the focal mechanisms the moment magnitudes
748 (M_{wr}) are the three largest regional earthquakes (event R1, R2, R3) that
749 are 126 – 178 km from the array. The small dashed box marks the array
750 location. In **(b)**, the colored circles are local events. The colors indicate
751 apparent stress drop ($\Delta\sigma$) based on the single-spectra measurements in
752 Kemna et al. (2020) (denoted as KN20). The size of the circles is pro-
753 portional to local magnitudes (0.01 – 3.0). The small black circles are
754 stations. The map shows the surface geology (see legend on the lower
755 left; Heran et al., 2003). In **(c)**, we show the corner frequency (f_c) esti-
756 mates using the single-spectra approach for a local event (event L1; the
757 magenta star marks the epicenter) in KN20. Each colored dot in **(c)** rep-
758 resents the median f_c measured by a subarray that includes stations
759 within a 2.5 km diameter circle.

824	9	Models with different attenuation assumptions fit the synthetic spectra well while the corner frequency estimates are off. Synthetic tests 2 <td>825</td> <td>(a) and 3 (b) use models (black dashed curves) without site attenuation ($\kappa = \kappa_{path}$) to fit synthetics (blue curves) generated including site attenuation ($\kappa = \kappa_{path} + \kappa_{site}$). The apparent f_c (blue lines) can deviate significantly from the true $f_c = 30$ Hz (red lines) with small fitting uncertainties (blue shades).</td> <td>21</td>	825	(a) and 3 (b) use models (black dashed curves) without site attenuation ($\kappa = \kappa_{path}$) to fit synthetics (blue curves) generated including site attenuation ($\kappa = \kappa_{path} + \kappa_{site}$). The apparent f_c (blue lines) can deviate significantly from the true $f_c = 30$ Hz (red lines) with small fitting uncertainties (blue shades).	21
826					
827					
828					
829					
830					
831	10	Relationship between apparent corner frequency (f_c) estimated ignoring site attenuation and the actual site attenuation (Q_s , left) and hypocentral distance (right). Synthetic tests 2 – 5 (a – d) assume $\kappa = \kappa_{path}$ with travel-time dependent attenuation to fit the synthetic spectra generated including site attenuation ($\kappa = \kappa_{path} + \kappa_{site}$). The median of the apparent f_c (blue dashed lines) deviate from the true f_c (30 Hz, red dashed lines). The deviation can be severe when κ increases (e.g., with lower S-wave velocity like in (d), or equivalently, with lower Q) and the source constraint n join the trade offs ($n = 3.5$, larger than the true value of 2). (e) is the measured f_c from actual data of event L1 in KN20. The gray scales indicate fitting uncertainty ((standard deviation of f_c)/ f_c x 100%). cc is Pearson's cross-correlation coefficient (all non-zero cc have p-values < 5%).	23		
832					
833					
834					
835					
836					
837					
838					
839					
840					
841					
842					
843					

Manuscript Received November 4, 2024